Masters Theses   Graduate School

8-2006

Vector Control and Experimental Evaluation of Permanent Magnet Synchronous Motors for HEVs

Timothy Adam Burress
University of Tennessee - Knoxville

Follow this and additional works at: https://trace.tennessee.edu/utk_gradthes

Part of the Electrical and Computer Engineering Commons

Recommended Citation

Burress, Timothy Adam, "Vector Control and Experimental Evaluation of Permanent Magnet Synchronous Motors for HEVs. " Master's Thesis, University of Tennessee, 2006.
https://trace.tennessee.edu/utk_gradthes/1517

To the Graduate Council:

I am submitting herewith a thesis written by Timothy Adam Burress entitled "Vector Control and Experimental Evaluation of Permanent Magnet Synchronous Motors for HEVs." I have examined the final electronic copy of this thesis for form and content and recommend that it be accepted in partial fulfillment of the requirements for the degree of Master of Science, with a major in Electrical Engineering.

<div align="right">Leon Tolbert, Major Professor</div>

We have read this thesis and recommend its acceptance:

Jack Lawler, Fangxing Li

<div align="right">Accepted for the Council:
Carolyn R. Hodges</div>

<div align="right">Vice Provost and Dean of the Graduate School</div>

(Original signatures are on file with official student records.)

To the Graduate Council:

I am submitting herewith a thesis written by Timothy Adam Burress entitled "Vector Control and Experimental Evaluation of Permanent Magnet Synchronous Motors for HEVs." I have examined the final electronic copy of this thesis for form and content and recommend that it be accepted in partial fulfillment of the requirements for the degree of Master of Science, with a major in Electrical Engineering.

<div align="right">

    Leon Tolbert
Major Professor

</div>

We have read this thesis
and recommend its acceptance:

    Jack Lawler

    Fangxing Li

<div align="right">

Accepted for the Council:

    Anne Mayhew
Vice Chancellor and
Dean of Graduate Studies

</div>

(Original signatures are on file with official student records.)

Vector Control and Experimental Evaluation of Permanent Magnet Synchronous Motors for HEVs

A Thesis Presented
For the Master of Science Degree
The University of Tennessee, Knoxville

Timothy Adam Burress

August 2006

Dedication

In Memory of Chris Tolbert

Acknowledgements

Abstract

The 2004 Toyota Prius exceeded sales expectations and led the automotive industry to realize that there is a healthy market for hybrid electric vehicles (HEVs). The Prius uses two interior permanent magnet motors to manipulate power flow throughout the drive system. Permanent magnet synchronous motors (PMSMs) are most suitable for HEVs and full electric vehicles due to their high efficiency, high power density, and fast dynamic response. This thesis will present vector control theory for PMSMs, with focus on interior permanent magnet motors.

The primary 50kW drive motor and inverter of the 2004 Toyota Prius Synergy drive system was removed for an intensive thermal, electrical, and mechanical evaluation in a dynamometer test cell at Oak Ridge National Laboratory. These evaluations include locked rotor, back-EMF, and motoring operation region tests. The resulting data is presented to reveal characteristics such as torque capabilities, thermal limitations, and motor efficiencies for all toque-speed operation points.

One of the most challenging tasks of the evaluation was to solve problems related to electromagnetic interference (EMI). The pulse width modulation (PWM) driven high voltage converter/inverter is a large source of electromagnetic field radiation and nearby low level signals, including control circuitry for the hybrid system, will experience EMI if proper countermeasures are not taken. Methods to reduce electromagnetic field radiation and practices to prevent EMI are discussed.

Table of Contents

List of Tables

List of Figures

Chapter 1

Introduction

Hybrid Electric Vehicles (HEVs) provide an opportunity to reduce dependency on foreign oil while decreasing the impact of harmful emissions on our environment and human health. The United States consumes about 7.3 billion barrels of oil, which is about 149 billion gallons of gasoline, per year. This is 25% of the world's oil production, and 56% of the total consumption is imported. Efforts are being made to increase U.S. oil production such as opening the Artic National Wildlife Refuge (ANWR) to oil and gas exploration. Even if this oil production option is economically feasible, there is still a long-term, global issue of dwindling oil supply.

Funding of research and development must be increased to improve the feasibility of alternative automotive systems. Since cars and light trucks account for about 45% of oil consumption in the U.S., great improvements of fuel efficiencies will have a substantial impact on oil importation and consumption. HEV and fuel cell technologies provide higher fuel efficiencies and are the stepping-stones to fully electric commercial vehicles in the future.

Optimal control and design of the electric machine ensures maximum operation efficiency of these alternative vehicles. These techniques and other methods that contribute to increased efficiencies, such as clever drive system configurations and control schemes, are presented in this thesis.

1.1 Advantages of HEVs

HEVs have higher fuel efficiencies than standard vehicles because they use an electric motor as a generator to apply torque when braking is needed. Therefore, the kinetic energy of a moving vehicle is translated into electrical energy that is stored in an energy storage device, typically a battery pack. Braking systems of conventional vehicles convert kinetic energy into heat through brake pad friction, which is dissipated into the surrounding environment. The energy stored in the battery pack is used to power an electric motor to drive the vehicle, typically through a DC/AC inverter, and possibly an additional DC/DC boost converter.

An additional benefit of the hybrid system is gained from the torque capability of permanent magnet synchronous motors (PMSMs). These motors, similar to all synchronous motors, have maximum torque output capability at very low speeds as shown in Figure 1.1. As seen in Figure 1.2, internal combustion engines (ICEs) must be operated at higher speeds, normally above 1500 rpm, to generate the torque needed to accelerate a vehicle. This is achieved through a clutching procedure in manual transmissions and a complex gear and clutch system in automatic transmissions.

The low speed, maximum torque capability of the electric motor in addition to benefit of regenerative braking make the HEV most effective in urban driving conditions, where braking and accelerating actions are required regularly.
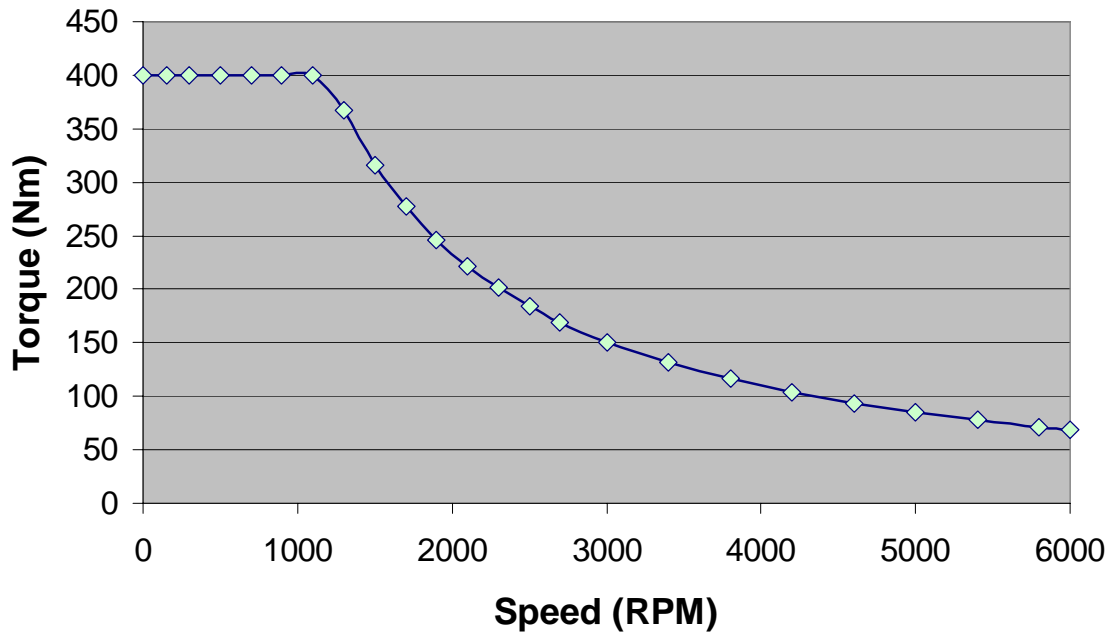
Figure 1.1. Exemplar PMSM maximum torque curve
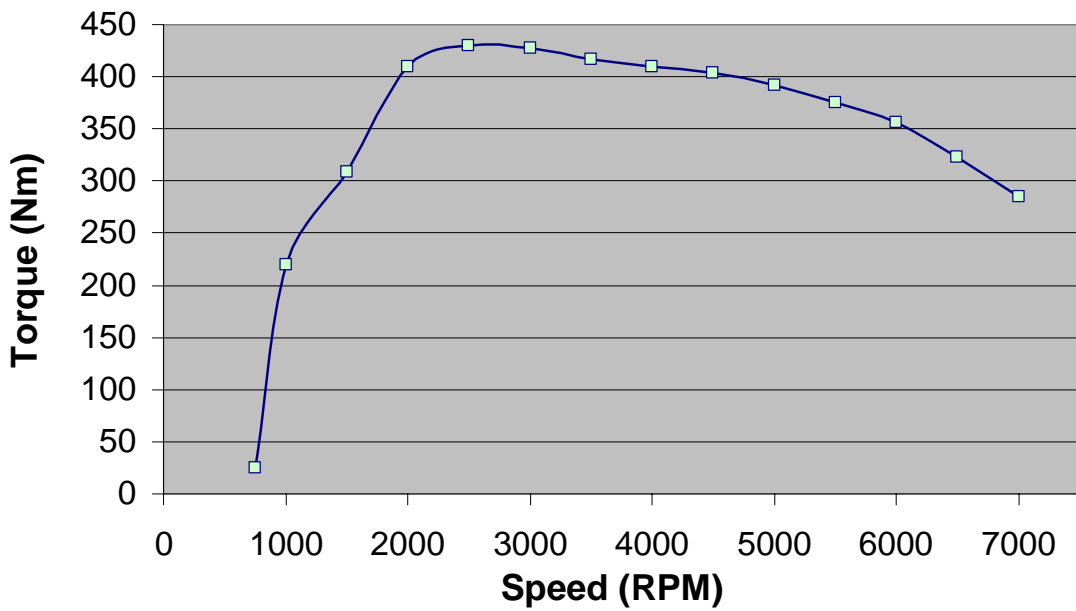
Figure 1.2. Exemplar ICE maximum torque and horsepower curves

The overall efficiency of a gasoline engine is only about twenty percent. In other words, only twenty percent of the thermal-energy in gasoline is transformed into mechanical work. Some drive systems, such as the 2004 Prius Synergy Drive, improve the overall gas engine efficiency by operating the engine in an optimal manner. The efficiency contour map of typical gasoline engine is shown in Figure 1.3 [1]. The most efficient operation points are at high torques and mid-range speeds. A drive system can be designed to allow the engine to operate in the most efficient regions more frequently. For example, consider a case when the engine is operating at a mid-range speed but the driving conditions require a low amount of torque. The efficiency of this operation point is typically low. If the required torque were higher, the corresponding efficiency would be higher. Therefore, a configuration that allows more torque to be applied by a generator will allow for a more efficient energy conversion, and the excess energy can be stored in a storage device such as a battery pack or super capacitor bank. Although Figure 1.4 shows that the inverter and PMSM efficiency map is much better than the gasoline engine efficiency map, a more realistic comparison is presented later.

The engine can be turned off when the vehicle is at low speeds or idling conditions. This is especially useful in metropolitan areas where traffic lights and congestion are common. Since an adequately sized electric motor has a much higher maximum torque capability than the gasoline engine at low speeds, the electric motor can be used to propel the vehicle until the engine is turned on at a particular speed. This method allows for the engine to be off during idle conditions, while providing an instant response to a torque command from the driver's acceleration pedal, without having to wait for the engine to be started.
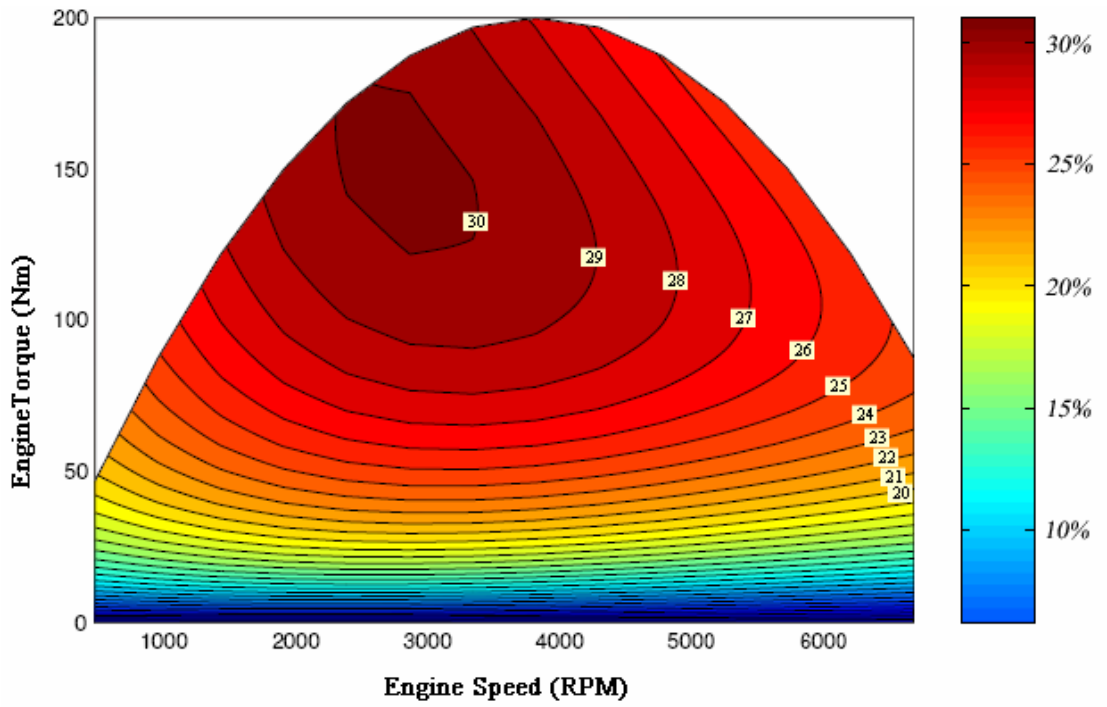
Figure 1.3. Exemplar gasoline engine efficiency map [1]
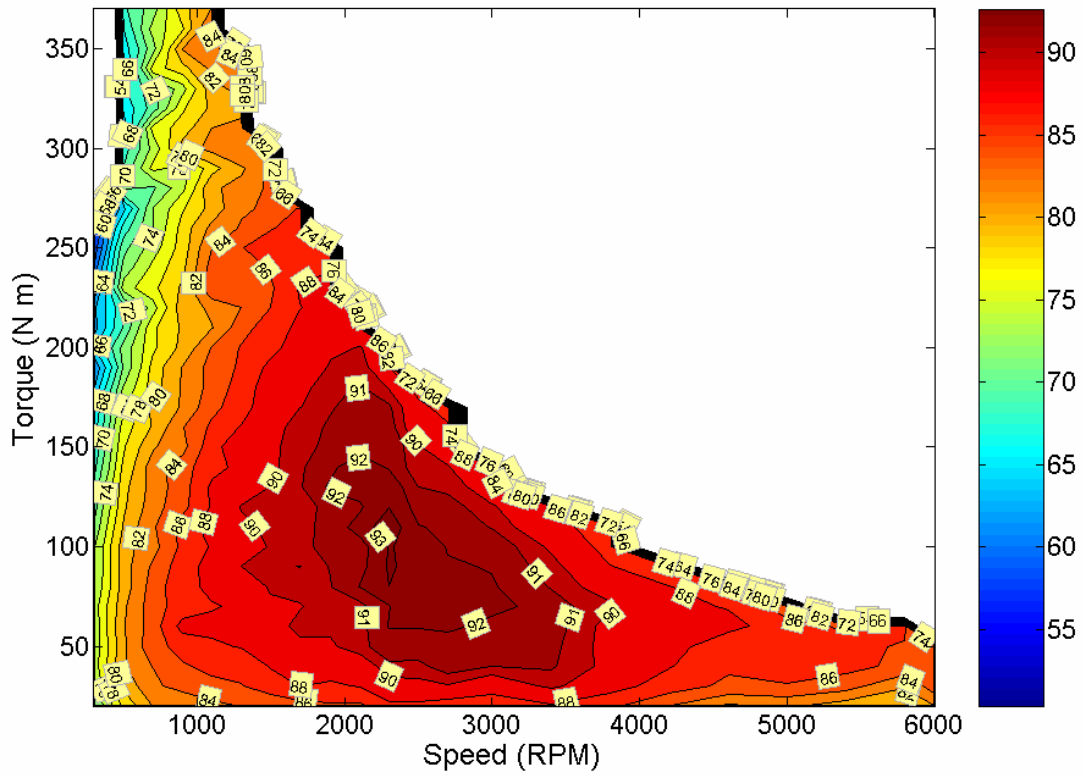
Figure 1.4. Exemplar Inverter and PMSM efficiency map

1.2 Disadvantages of HEVs

There are very few negative aspects of HEVs. The electric motor or gas engine alone can propel a full hybrid electric vehicle. Since full HEVs use the motor and gas engine coincidently, the size of the engine is often designed to be smaller than that of a comparably sized vehicle due to the extra torque available from the electric motor. Additionally, using a smaller engine will result in higher fuel efficiencies. However, if the battery pack has a low state of charge, then only the gas engine can meet torque demands. This is especially an issue for highway driving, where significant power demands are required for extensive times. The 2004 Toyota Prius Synergy drive system configuration allows for the battery to be charged as long as high torques are not needed at the drive wheels. Then when heavy acceleration is needed, during passing for example, large instantaneous power requirements will be able to be met.

Replacement costs of storage components are also a concern. For example, battery packs for HEVs currently on the market range from $2000 to $5000 and need to be replaced in about 8 to 10 years. As HEVs become more widely used, an environmentally responsible and economical means of disposing or recycling these battery packs will be needed. Additionally, although precautionary safety countermeasures are implemented, high voltages are present throughout the vehicle. The prevalent threat of these high voltages is not for human health, but possible electromagnetic interference (EMI) in signals in or near the vehicle. It is highly unlikely that shock or any other related injury would be received from an HEV power source.

1.3 System Efficiencies

The typical range of a vehicle is about 300 to 500 miles, and the petroleum infrastructure provides an easy means to quickly replenish stored energy in a vehicle. Currently, HEVs primarily use this infrastructure, and thus they do not require a novel or modified means of obtaining energy. A "plug in hybrid" uses the power grid to recharge the battery pack. Some individuals think that using the power grid to fuel full electric vehicles is an immediate solution to our problem with emissions and fossil fuel consumption. It is important to realize that replenishing energy levels through the power grid does not completely avoid harmful emissions. About 67% percent of the electricity in the United States is generated from the combustion of fossil fuels. To receive substantial environmental benefits, use of cleaner energy sources such as hydroelectric or nuclear power generation must be increased. Additionally, if full electric vehicles become the crux of transportation, significant changes to the means of power distribution and generation will be needed since the load demand would increase significantly.

Research and development in areas of HEV technology will lead to improvements that will also help to achieve the production of a fully electric commercial vehicle. To produce a full electric vehicle in commercial form, the most profound obstacle to overcome is the low energy density of today's storage components. After technological improvements are made, advantageous characteristics of various devices, including fuel cells, ultra capacitors, and/or batteries, can be combined to power electric vehicles.

It is essential to maximize the efficiency of each component in the process of converting fuel to mechanical work. The contours in the efficiency contour map in Figure 1.4 represent the efficiency for various torques and speeds for both the DC/AC inverter and PM motor combined. The average efficiency depends on driving behavior, but can be approximated to be about 80%. This seems substantially better than the 20% efficiency of the gasoline engine, but an analysis of various conversion processes from the fuel source to the vehicle reveals a much smaller difference of efficiency.

Lead-acid battery packs are the most common type of energy storage currently implemented in HEVs and full electric vehicles. The efficiency of a battery fluctuates with many variables such as temperature, current demand, and state of charge. Lead-acid batteries have an average efficiency of about 90%. If the battery pack is recharged via the power grid, an AC to DC rectifier is required. Typical efficiencies for rectifiers are about 90 to 95%. If fossil free energy sources such as nuclear or hydroelectric generation are used, the overall efficiency is about 68%. However, if the electricity is generated through combustion processes, this efficiency is decreases by about 40% to give an overall efficiency of 27%.

A major limitation of using batteries as the primary source of energy for a vehicle is that they have much lower energy densities than gasoline. Thus, it is difficult to design a robust electric vehicle to match the 300 to 500 mile range of a conventional vehicle. A secondary issue is the time involved with recharging the battery pack, which is typically much longer than the time it takes to refill a standard size gasoline tank. Combining energy storage components may be the key to meeting these criterions.

Fuel cells make use of the flow of charge that occurs during the conversion of hydrogen to water and heat via the polymer electrolyte membrane. This process is essentially emission free, but hydrogen is most commonly obtained from natural gas or methanol reformation, so fossil fuel consumption is not eliminated. Reformers can be utilized in a bulk supply system, similar to the gasoline structure, or they may also be utilized on a more local level, at vehicle refueling stations for example. A reformer can even be implemented onboard a vehicle. The energy conversion efficiency of onboard reformers is about 40 to 50%. The latter methods may be most plausible for distribution since hydrogen has a very low energy density when compared to gasoline. These methods allow for natural gas or methanol to be distributed via existing infrastructures. Liquid hydrogen has a very high energy density, but requires a storage pressure of about 5,000 psi, which is difficult to safely implement in a vehicle design.

Hydrogen can also be produced through the electrolysis of water. This method is more considerate for our environment and limited natural resources if the electricity used during this process is generated using clean or renewable resources such as solar, wind, hydroelectric, or nuclear power generation. With this in consideration, if the costs and maintenance requirements associated with the fuel cell can be decreased, this is one alternative to relieve problems with conventional automotive systems. One drawback to the fuel cell is that it is does not permit bidirectional power flow. Therefore, regenerative braking is not possible unless additional storage components are used.

A summary of various system efficiencies is shown in Figure 1.5 [2,3]. These calculations are only rough approximations and do not portray a detailed comparison of efficiency or feasibility of each system. They are presented to emphasize the importance of maximizing the motor and inverter efficiencies, regardless of the energy source. Note that energy from regenerative braking in the HEV experiences two transformations before reaching the drive wheels, from mechanical to electrical energy, and then back to mechanical energy. This further stresses the importance of motor and inverter efficiencies. This thesis will mostly discuss design and control methods to maximize motor efficiencies. In addition to optimal motor control, clever drive system designs are also important in maximizing total efficiency.

Conventional Vehicle

20%
Gasoline Engine

Full Hybrid Electrc Vehicle

20%   ✖   1.7   ⟶   34%
Gasoline Engine   Regenerative   Full
                   braking   HEV

Battery Powered Electric Vehicle - (fossil fuel combustion)

40% ⟶ 95% ⟶ 90% ⟶ 80% ⟶ 27%

Fossil fuel   AC to DC   Battery   Inverter
to electricity rectification storage   and motor

Battery Powered Electric Vehicle - (Nuclear, hydroelectric, etc.)

95% ⟶ 90% ⟶ 80% ⟶ 68%

AC to DC   Battery   Inverter
rectification storage   and motor

Fuel Cell Powered Electric Vehicle

40% ⟶ 75% ⟶ 80% ⟶ 24%

Reformer   Fuel   Inverter
(at vehicle   cell   and motor
level)

Figure 1.5. Comparison of efficiencies for various fuel sources [2,3]

10

1.4 Thesis Outline

The primary goal of this thesis is to present a method to model and optimally control an interior PMSM and to discuss the challenges and results of implementing these methods to test the primary inverter and motor of the 2004 Toyota Prius. The Prius Synergy Drive system is discussed along with other drive systems and control techniques. A model and control method for the interior PMSM is developed in the rotating two-phase *d-q* frame of reference, which significantly simplifies the mathematical rigor involved with the standard three-phase system. The 2004 Prius boost converter, inverter, and motor were extensively tested to reveal characteristics such as thermal limitations, continuous torque capabilities, and motor efficiencies.

1.5 Chapter Outlines

Chapter 2 discusses the 2004 Prius Synergy Drive and pertinent information.

Chapter 3 presents modeling and control methods for PMSMs.

Chapter 4 explains the experimental setup which includes data acquisition and control system interfacing.

Chapter 5 presents the results from implementation of the presented control method.

Chapter 6 provides conclusions and recommendations for future work.

Chapter 2

HEV Drive Systems

All hybrid electric vehicles (HEVs) have at least two components that contribute to providing power to the drive wheels. The most common components used in today's HEVs are battery driven electric motors and internal combustion engines (ICEs). Most HEVs fall into one of two main categories based on their power train configuration. An HEV with a series configuration uses an electric motor to apply all power to the drive wheels, while an ICE spins a generator to power the drive motor and maintain stored energy levels, typically in a battery pack. This configuration is not common in automotive applications since the generator and drive motor must be adequately sized for high power demands. The parallel configuration is the most common, where the ICE and at least one electric motor directly supply power to the drive train.

There are several sub-categories of series and parallel configurations, which are designated by the size of the electric motor and ICE. Assist hybrids are very similar to conventional vehicles, yet a small electric motor is used for extra power when heavy acceleration is desired. Assist hybrids do not provide a significant improvement on fuel efficiency. Mild hybrids have a slightly larger electric motor that is used for regenerative braking and starting the ICE after coasting or idling. Full hybrids have large electric motors and can be powered by the electric motor or ICE alone. These hybrids have a substantial improvement of fuel efficiency.

2.1 The 2004 Toyota Prius Synergy Drive System

The 2004 Toyota Prius set the standard for HEVs as it established a large and healthy market with its eco-friendly fuel efficiency average of about 55 miles per gallon. The Prius uses the Synergy Drive System to achieve higher efficiencies through regenerative braking and other clever techniques. The primary mechanical component of the Synergy Drive is the planetary gear shown in Figure 2.1 [4]. It provides a mechanical interface between the 50 kW drive motor, 30 kW generator, and 1.6-liter gasoline engine. The 30 kW generator is connected to the innermost component called the sun gear. Four small "planet" gears are located between the sun gear and the outermost component, the ring gear. A carrier connects the four planet gears to the gasoline engine. The 50 kW motor is connected to the ring gear as well as the drive wheels through a torque increasing gear ratio.

Although the operation speed of the 50 kW motor must vary linearly with the speed of the vehicle, the amount of torque applied by the motor and ICE can be varied if the engine and generator speeds are adjusted properly. This allows the system to be designed so that the engine operates most efficiently for common torques and speeds required by the drive wheels, shown in Figure 2.2. This system is a type of continuously variable transmission (CVT), since the speed and torque applied to the drive wheels can be varied using only one gear configuration. Additionally, compared with a conventional transmission, gear losses are greatly reduced due to the simplicity of this design. Note that this CVT is different from the traditional forms of CVTs, such as frictional or cone and belt types.

13
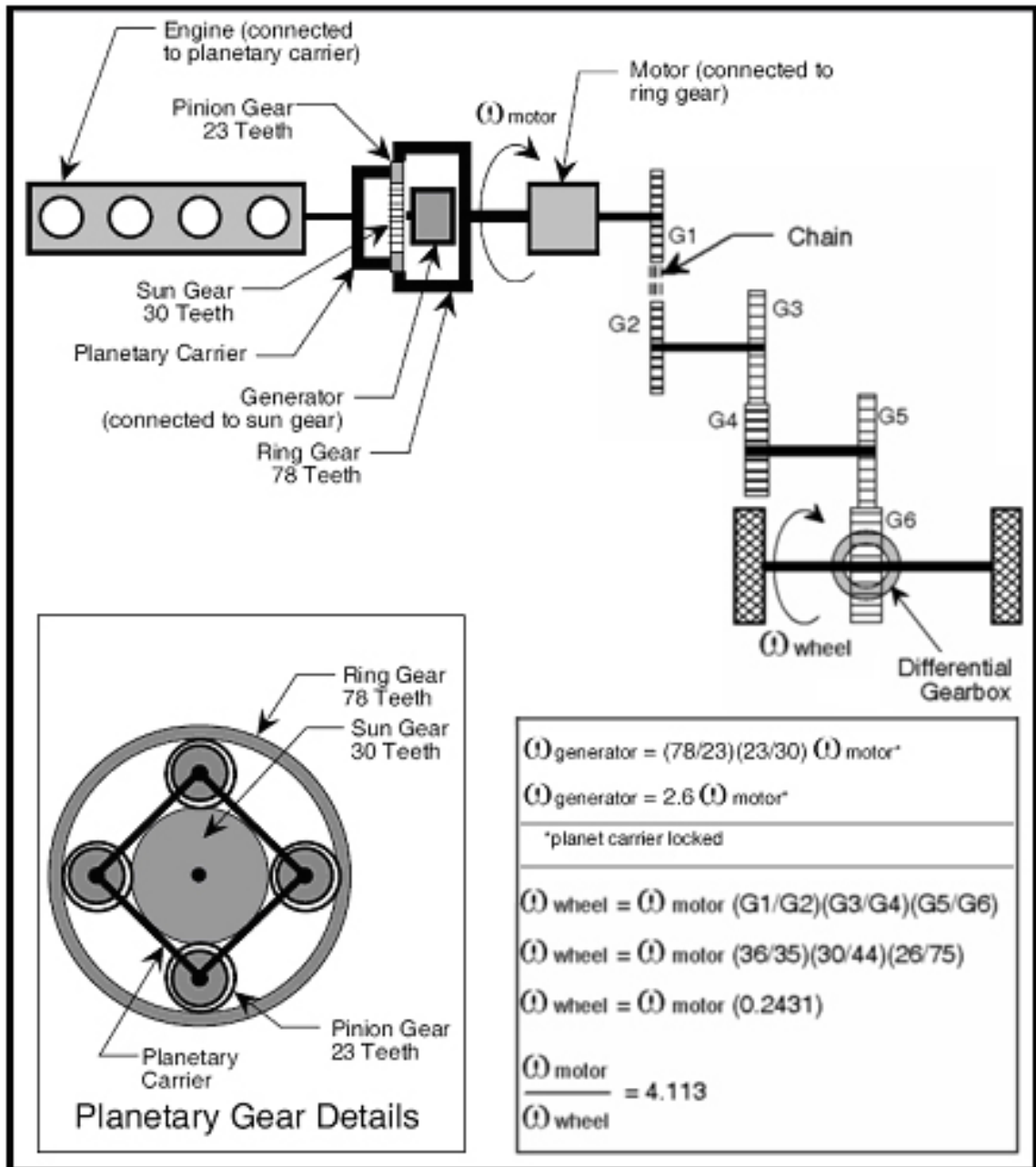
Figure 2.1. Prius planetary gear system [4]
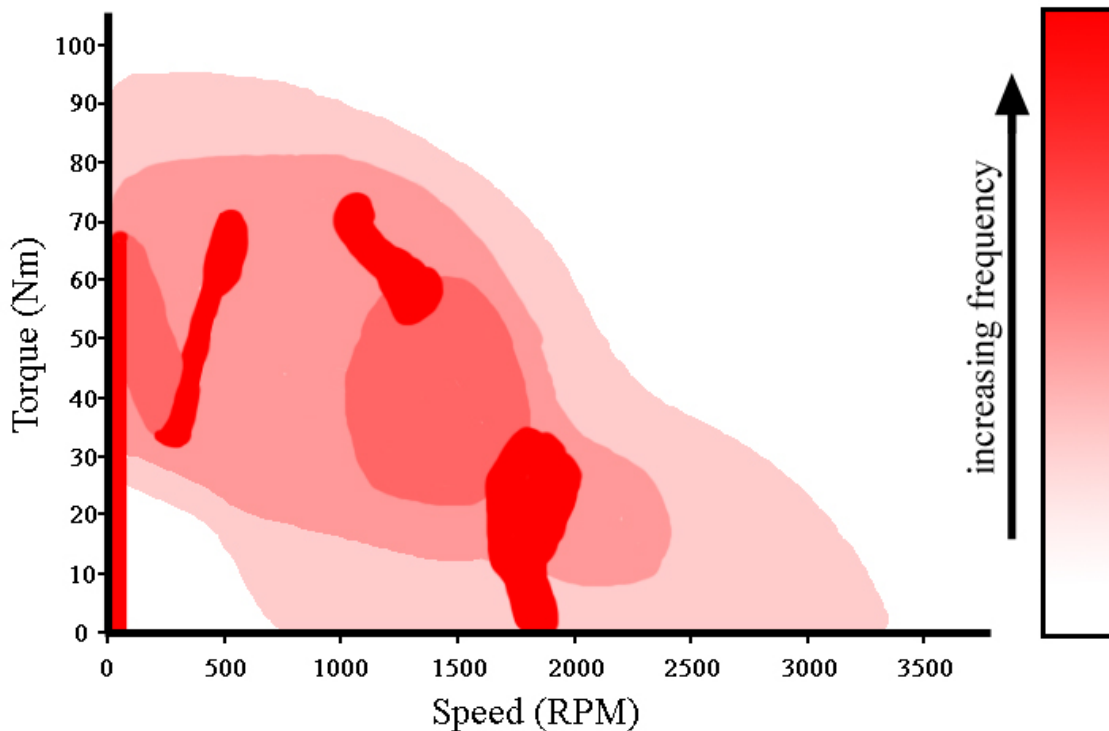
Figure 2.2. Frequent city driving torques and speeds required at motor shaft

The planetary gear system in the Prius is also known as a power split device because it is capable of splitting the power required by drive wheels among two (or three) power sources. Additionally, the motor and generator inverters share the same DC bus, which creates an opportunity for many power flow schemes, which are described in Figure 2.3 [5,6]. One very important aspect of this system is that the drive wheels can be driven solely by the gasoline engine or electric motor, making it a full hybrid. As shown in Figure 2.3, the Synergy Drive system can function as a series or parallel power train configuration. Furthermore, the energy level of the battery pack can be replenished while driving, braking, and idling.

	Charge At standstill, the battery pack is charged if the energy level is low, or if heat is needed for the catalytic converter or for comfort in the interior compartment.
	Battery Drive If the battery pack has sufficient energy, the vehicle is propelled only by the battery pack, particularly for low speeds and reverse driving.
	Engine & Motor Drive This mode of operation is used for moderate acceleration, and the configuration enables the engine to be operated in more efficient operation regions.
	Engine Drive With Charge If vast power demands are not needed at the drive wheels, such as for highway driving, the engine is operated in efficient regions while recharging the battery pack.
	Engine and Motor Drive With Charge This mode of operation is used for heavy power demands, which are for example associated with the climbing of steep hills, while also recharging the battery pack.
	Full Power or Gradual Slowing Power is obtained from the engine and battery pack for maximum power demands. This configuration is also used during slight deceleration to reduce gas consumption.
	Regeneration Through Braking When the brake pedal is pressed, the vehicle speed is reduced as kinetic energy is transformed into electrical energy, which is stored in the battery pack.

Figure 2.3. Prius power flow configurations [5,6]

The Prius can lightly accelerate up to 42 miles per hour (MPH) while being propelled by the primary drive motor and battery pack alone, this is known as the stealth mode. The system can even operate in the stealth mode at very high speeds if the driving terrain contains a significant decrease in elevation. However, for ordinary acceleration levels and driving conditions, the engine is engaged at a much lower speed and continues to operate at high speeds.

The most significant limitation that prevents operation in stealth mode at very high speeds is the 20 kW power rating of the battery pack and boost converter. A diagram of the electrical drive portion of the Synergy Drive is shown in Figure 2.4 [5]. The rated torque and power curves for the primary electric motor are shown in Figure 2.5 [7] and Figure 2.6 [7] respectively. Although the 50 kW motor is capable of producing more torque at high speeds, the engine must be spinning the 30 kW generator to add to the 20 kW available from the battery pack.
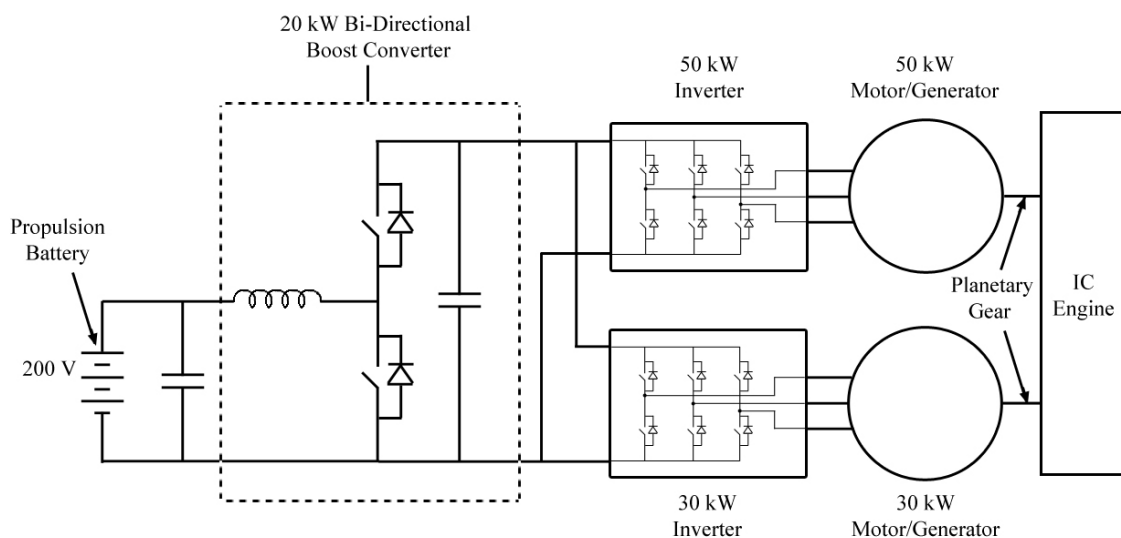
Figure 2.4. Prius electrical drive system diagram [5]
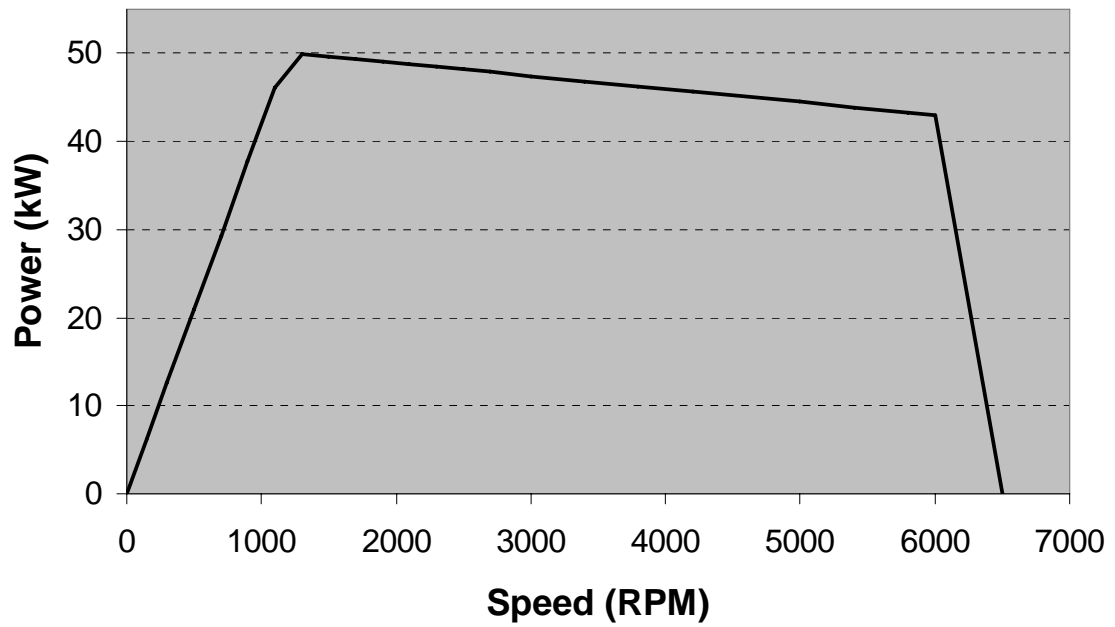
Figure 2.5. 2004 Prius maximum power output [7]
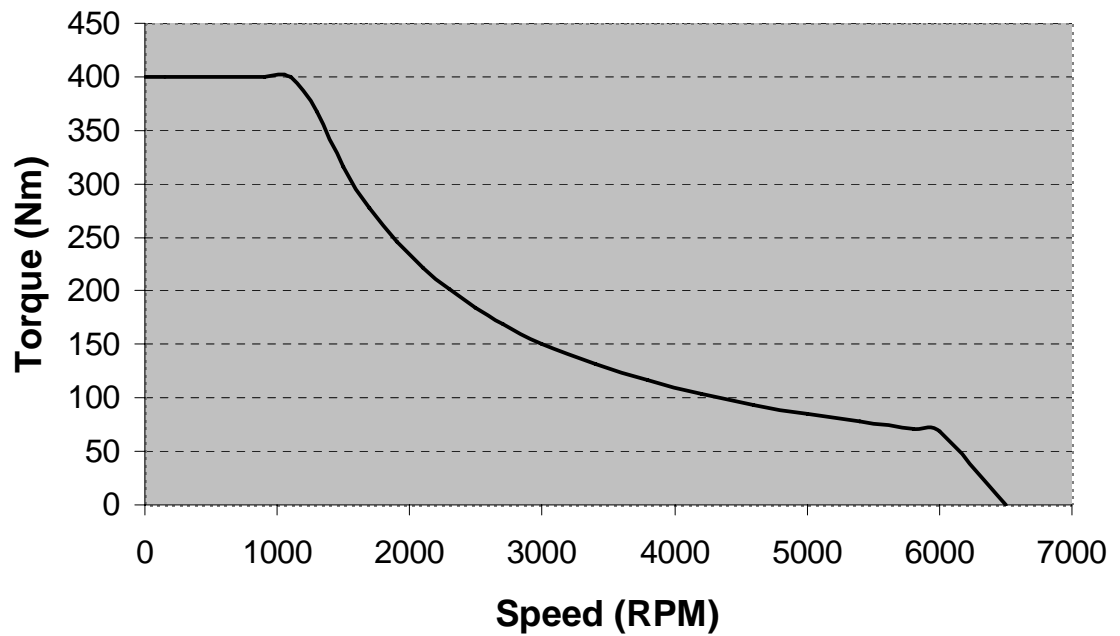
Figure 2.6. 2004 Prius maximum torque output [7]

18

A summary of characteristics for the Prius drive components is shown in Table 2.1 [5]. The primary 50 kW electric motor is capable of producing a rated torque of about 400 Nm up to a base speed near 1200 rpm. Thermal limits are violated after operating under these conditions for a very short amount of time. The most restrictive temperature limit is determined by the type of insulation used on stator windings. The Prius has Class F conductors for its windings, which permit operation temperatures up to 185 ºC. Oil is used for cooling and lubrication of the motor, generator, and gears. To extract heat, a water and ethylene glycol coolant mixture flows from the radiator through the inverter casing and motor casing, independent of the ICE coolant loop.

Table 2.1. 2004 Prius drive component specifications [5]

Component	Property	Property Value
Gasoline Engine	Type Maximum Power Maximum Torque	1.5 liter DOHC, 4 cylinder 57 kW (76 hp) at 5000 rpm 111 Nm (82 lb. ft.) at 4200 rpm
Motor	Type Maximum Power Maximum Torque	PMSM 50 kW (67 hp) for 1200-1540 rpm 400 Nm (295 lb. ft.) for 0-1200 rpm
System	Maximum Power Maximum Torque	82 kW (110 hp) 478 Nm below 14 miles per hour
Battery	Type Assembly Voltage Power Output Estimated Lifetime	Nickel-metal hydride 28 - 7.2 V cells in series 201.6 V 21 kW 150,000 miles

2.2 Variable DC Bus Voltage Using Boost Converter

The permanent magnets of the rotor induce a voltage in the stator windings that is proportional to the rotor speed, known as back-EMF voltage. The Prius uses a boost converter to increase the DC bus voltage of the inverter to overcome the contrary effects of induced back-EMF voltage at high speeds. This is sometimes misleadingly termed as a floating DC bus since the DC bus voltage can be varied. The currents through the IGBTs in the Prius inverter are regulated by PWM signals. For a maximum voltage to be applied to the motor, the PWM command signals are over-modulated, resulting in square-wave stator phase voltages. The maximum fundamental component of the phase voltage, through Fourier expansion, can be expressed by

$$V_{LN(RMS)_{\max}} = \frac{1}{\sqrt{2}} \frac{4}{\pi} \frac{V_{dc}}{2} = 0.45 V_{dc}. \tag{2.1}$$

According to (2.1) and excluding the boost converter, the Prius battery voltage of 201.6 V produces a maximum phase voltage of 90.8 V. The back-EMF voltages of the Prius, shown in Figure 2.7, were measured by spinning the rotor with a separate motor, without power applied to the Prius motor leads. Without flux weakening or other high-speed control techniques, the maximum attainable speed with a battery voltage of 201.6 V is only about 1000 rpm. Beyond this speed, the inverter cannot force current through the windings because the back-EMF voltage is greater than the supply voltage. Therefore, a boost converter is used to increase the DC bus voltage to 500 V, which increases the maximum RMS phase voltage to 225.1 V. The maximum speed for this voltage is about 2500 rpm. Note again that this is not the case if a high-speed control technique is used.
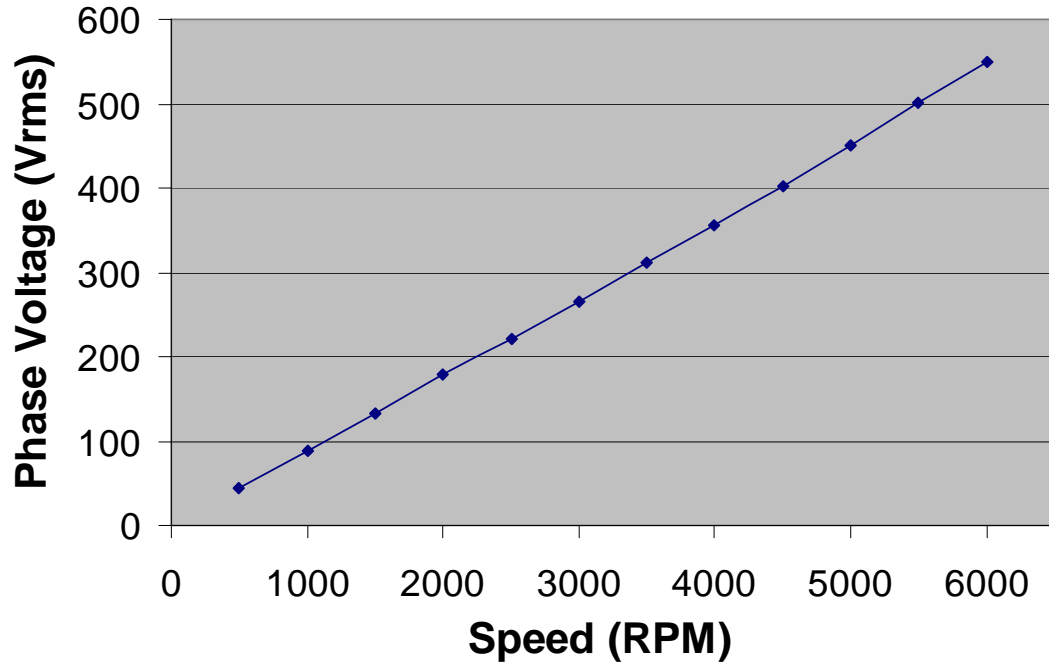
Figure 2.7. Prius back-EMF phase voltage

The output voltage of the boost converter is controlled by a PWM signal and is varied in order to obtain the most efficient operation. If high voltages are not needed, the voltage is decreased to reduce leakage and switching losses. In addition to increasing the voltage to overcome induced back-EMF, the voltage is increased to minimize stator current and operating temperature for large power demands.

The maximum speeds mentioned above are for no-load conditions. If more torque is applied to the motor at these speeds, the inverter cannot provide enough voltage to force a torque-producing current through the windings. Thus, in Chapter 3, a flux-weakening control method is discussed that opposes the flux produced by the permanent magnets and effectively decreases the magnitude of the induced back-EMF voltage

2.3 Summary

The multiple power flow configurations of the Prius Synergy Drive system provide the means for the vehicle to be driven by the electric motor or gasoline engine independently or both can be utilized simultaneously. While some benefits of the system are gained during highway driving, they are substantially reaped during city driving conditions, where more energy can be harvested through regenerative braking and the low-speed torque capabilities of the electric motor are prominent.

The boost converter and 50 kW inverter and motor, with anticipated performance ratings defined in Figures 2.5 and 2.6, have been removed from the system for evaluation. Even with a boosted DC bus voltage of 500 V, a flux-weakening control method presented in Chapter 3 is used to counteract the PM flux in order to reduce the back-EMF voltage for moderately high speed operations.

Chapter 3

Modeling and Control of PM Motors

An optimal control algorithm is essential for attaining high efficiencies and maximum torque per current for a wide speed range. Developing an accurate model and optimal controller for a permanent magnet (PM) machine can be very burdensome. These tasks require accurate knowledge of the machine parameters, which may be difficult to measure or predict and may vary with temperature, current, speed, etc. Making approximations such as neglecting iron saturation or flux linkage harmonics simplifies a motor model significantly. The validity of these approximations and the required parameter accuracy varies based on the design and application. Therefore, a model or controller development approach may vary even within a particular species of PM machine. In this application, evaluations of the system are being made in steady state and an optimal dynamic response is not needed, yet a sophisticated controller is required.

In PM motors, a back-EMF voltage is induced in the stator windings as the rotor rotates and causes the flux through the stator windings due to the permanent magnets to vary. As the magnitude of the rotor speed increases, the flux through the stator windings changes more rapidly and therefore more voltage is induced. Without the appropriate counter measures, the back-EMF voltage will exceed the maximum voltage available from the inverter and DC supply. Thus, a field oriented control method is used at high speeds to oppose the PM flux in order to reduce the back-EMF.

3.1 PM Machine Classifications

Permanent magnet (PM) motors are often classified according to magnet position, presence of reluctance, and shape of back-EMF voltage waveform. The basic shape of the back-EMF waveform is predominantly determined by the stator winding distribution. A trapezoidal back-EMF PM machine has concentrated windings, as opposed to having sinusoidally distributed windings, as shown in Figure 3.1 [8]. The nomenclature often associated with these motors can be misleading. Motors with a trapezoidal back-EMF waveform are referred to as brushless DC machines (BDCMs), although both species (sinusoidal and trapezoidal) are brushless and operate as AC machines. Motors with sinusoidal back-EMF waveforms are referred to as permanent magnet synchronous motors (PMSMs), although both species have permanent magnets that are synchronized with the rotating stator flux.
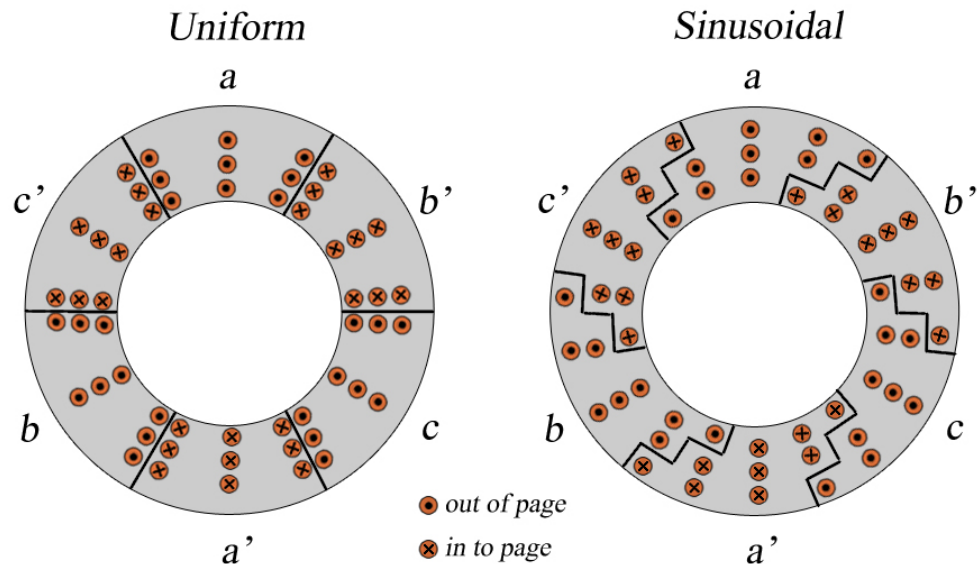
Figure 3.1. Uniformly and sinusoidally distributed stator windings [8]

Since trapezoidal back-EMF machines have concentrated windings, the flux through the stator winding due to the permanent magnet is more uniform than in a machine with sinusoidally distributed stator windings. Therefore, the back-EMF waveform appears to be trapezoidal and has flat peak with a long duration. This can be seen by comparing the measured sinusoidal back-EMF voltage with a simulated trapezoidal back-EMF voltage, shown in Figure 3.2 and Figure 3.3 respectively. An important distinction between the sinusoidal and trapezoidal back-EMF waveforms is the duration of the peak voltage, which is much longer for the trapezoidal waveform in this case. The peak voltage duration of the trapezoidal waveform is typically 120 electrical degrees.
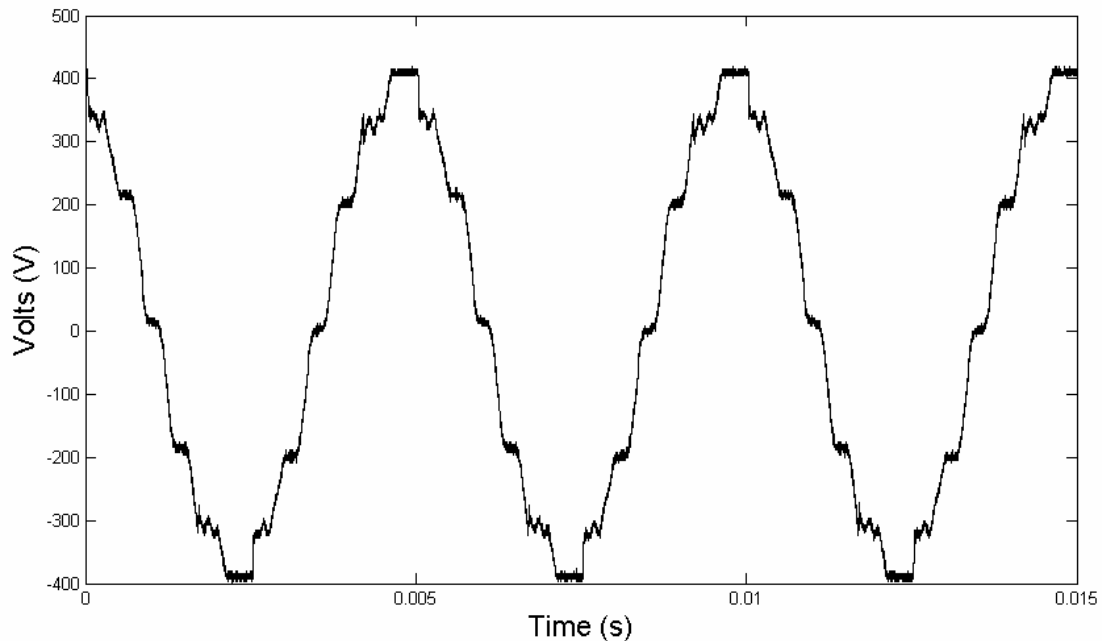
Figure 3.2. Measured sinusoidal back-EMF voltage
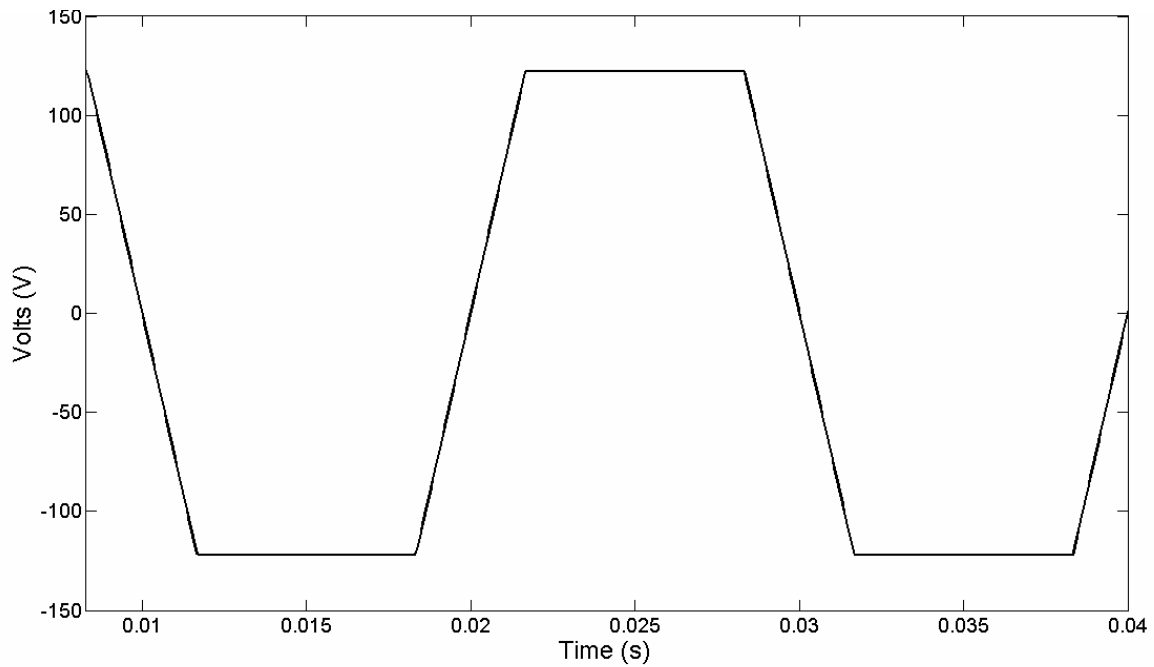
Figure 3.3. Simulated trapezoidal back-EMF voltage

Although the sinusoidal back-EMF voltage waveform in Figure 3.2 seems to have some non-sinusoidal tendencies, the fundamental component is much larger than the harmonics according to the fast Fourier transform (FFT) shown in Figure 3.4. The flux linkage harmonics are closely associated with the back-EMF voltage harmonics, and for the sinusoidally wound PM machine, they can be neglected without greatly degrading the quality of the model. The FFT of the simulated trapezoidal back-EMF voltage is shown in Figure 3.5. While the waveforms appear to be similar, the Fourier analysis reveals that if the flux linkage harmonics of the trapezoidal back-EMF PM machine are neglected, a significant amount of error may be incurred since these harmonics affect the stator currents and torque output. In HEVs, the stator is typically sinusoidally wound to attain a higher performance and to avoid torque ripple.

26
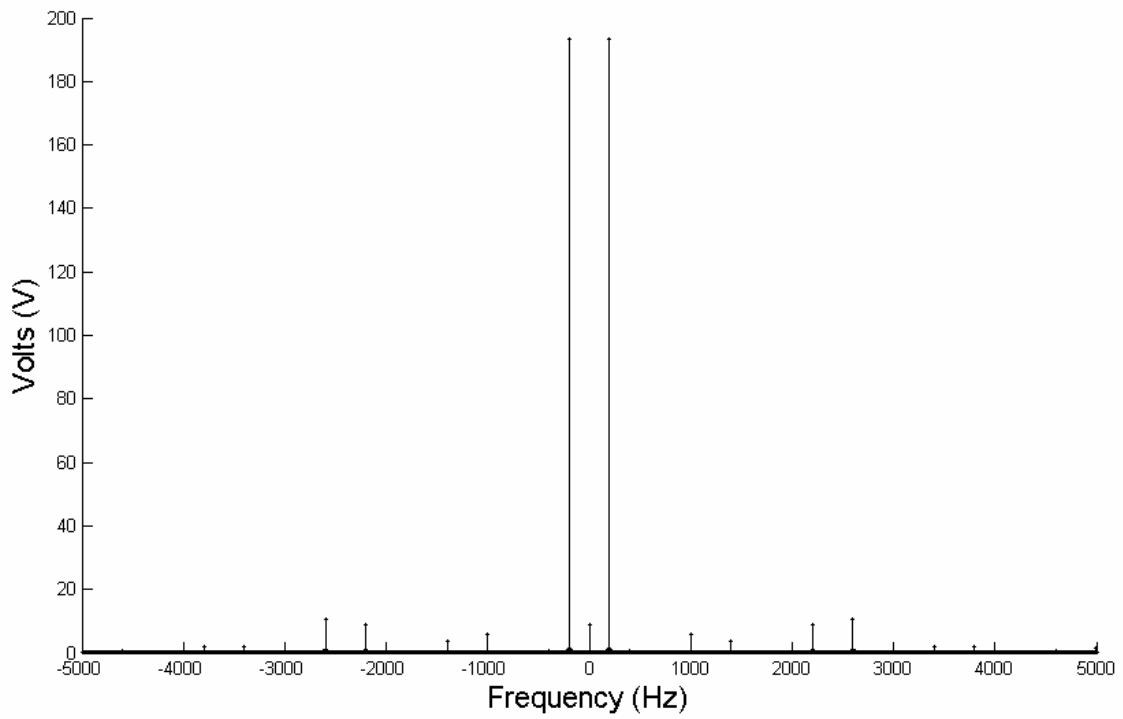
Figure 3.4. FFT of sinusoidal back-EMF voltage
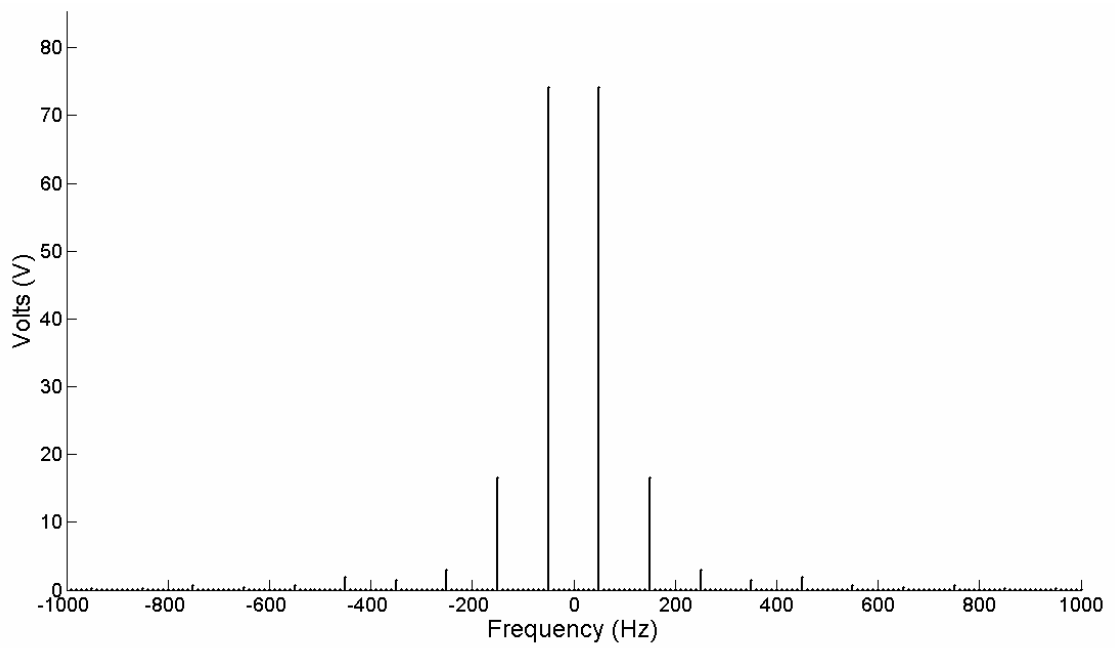
Figure 3.5. FFT of trapezoidal back-EMF voltage

27

Permanent magnet (PM) motors are also classified by the manner in which the magnets are positioned. Two primary classifications of PM motors with regard to magnet location and orientation are surface permanent magnet (SPM) and interior permanent magnet (IPM) motors, shown in Figure 3.6 [9]. The SPM design consists of magnets that are mounted on the surface of the rotor, while the IPM design has magnets contained within the rotor. Therefore, the mechanical integrity of the IPM machine is superior to that of the SPM machine since it is easier to secure the magnets, which are subject to centrifugal forces from rotation as well as intensive transients due to magnetic forces. This mechanical security is especially important in motors with rotor speeds above 10,000 rpm, which are currently available in commercial HEVs.
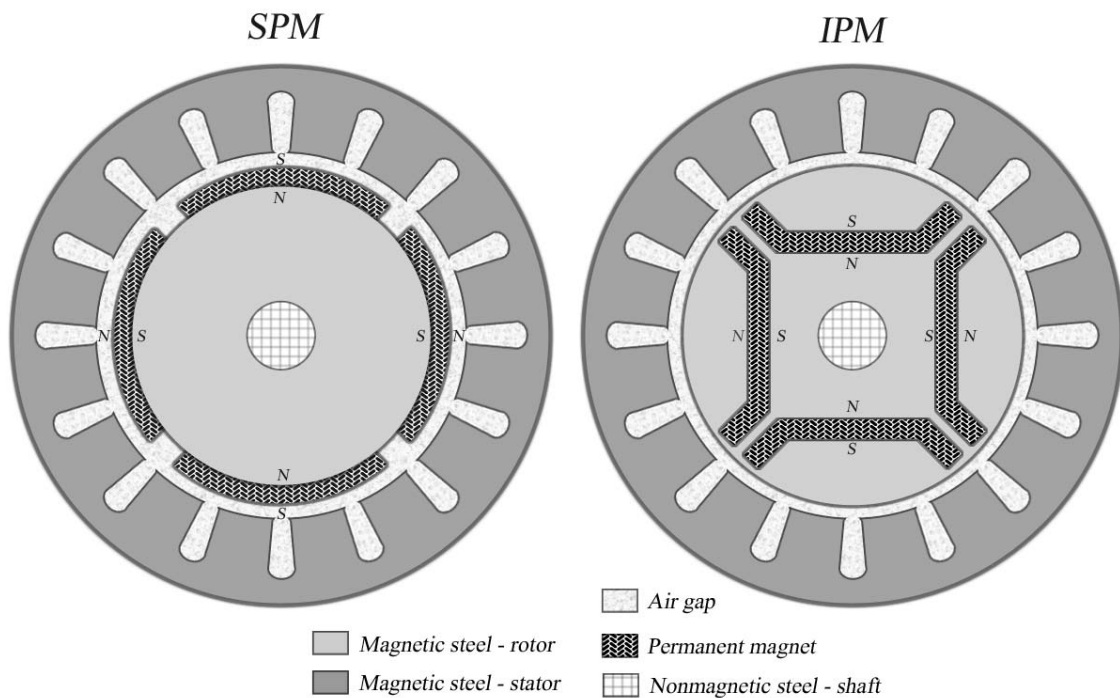
Figure 3.6. Interior and surface PM machine cross-sections [9]

Another means of classifying PM motors is related to magnet location. Surface permanent magnet (SPM) machines are typically non-salient, meaning that the permeance of rotor does not vary significantly around the circumference. In an SPM, flux generated by current in the stator windings must pass through the air gap, PM, and steel rotor to complete the magnetic circuit [9], as shown in Figure 3.7. When compared to magnetic materials such as iron or steel, the permeability of the PM material is very small and is about the same as that of air. Consequently, the permeance of the rotor is substantially limited by the air gap and magnet material. The permeance varies in the rotor of interior permanent magnet (IPM) machines since flux paths that do not include the PM are available at some angles, as shown in Figure 3.7. Therefore, IPM machines are referred as salient, and with saliency, a new torque component accompanies the already existing PM torque, discussed further in section 3.5.
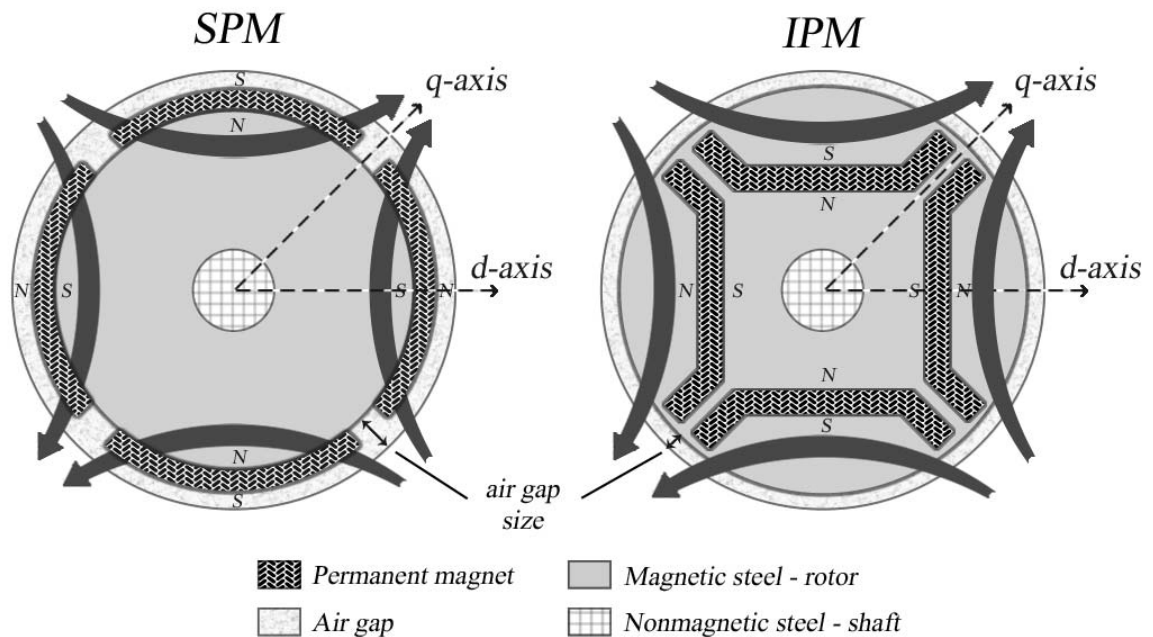
Figure 3.7. Possible flux paths of SPM and IPM machines [9]

3.2 A Three-Phase Model of the Non-Salient PM Machine

Most PM machine research and development is presently focused on salient IPM machines since they are mechanically more reliable, offer more torque for less PM material, and have better flux weakening capabilities, and thus higher speed ranges than non-salient SPM machines. A model will first be developed for a sinusoidally wound non-salient SPM machine in the traditional three-phase domain with a stationary reference. Then, a transformation, called the *d-q* transformation, is applied to simplify the model into a two-phase domain with a reference that rotates with the rotor. Subsequently, the non-salient PM machine model will be modified to incorporate saliency since the concept and effects of saliency are more easily understood in the *d-q* frame of reference. Additionally, the mathematical model is less complex because sinusoids are eliminated using the rotating reference.

A model of the three phase non-salient PM machine will be developed while assuming an ideal sinusoidal winding distribution and neglecting flux linkage harmonics, core losses, and iron saturation. It will be assumed that the machine parameters are constant and do not vary with current, temperature, speed, etc. These simplifying assumptions can result in a significant amount of error for particular operating conditions, which will be discussed later. The three-phase non-salient PMSM equivalent circuit model is shown in Figure 3.8.
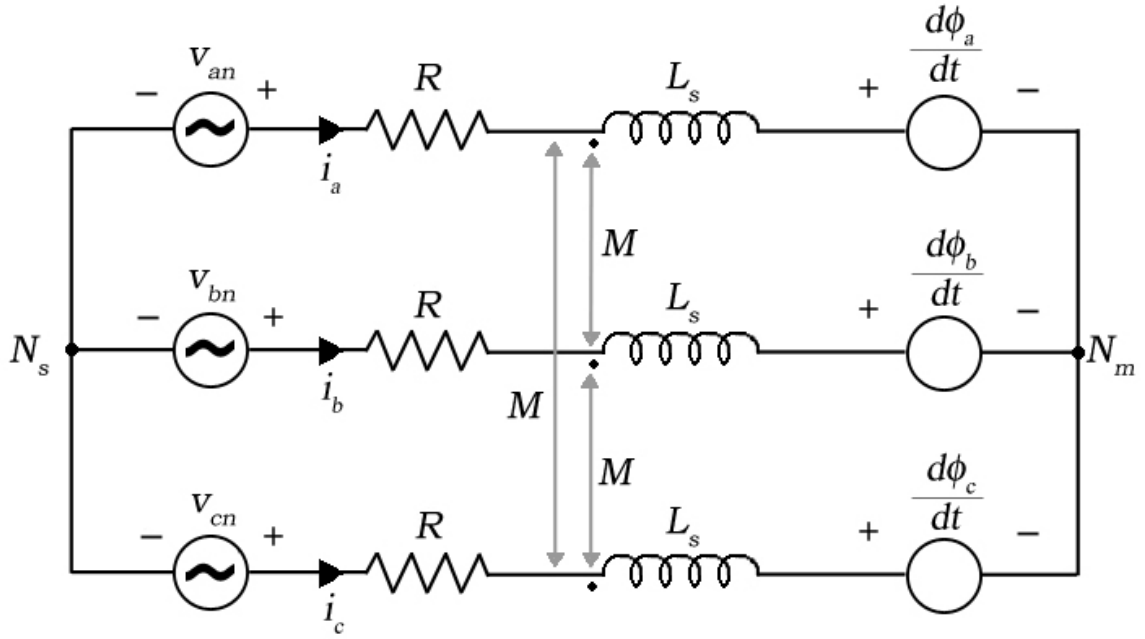
Figure 3.8. Three-phase non-salient PMSM equivalent circuit

where

i_a, i_b, and i_c represent the phase currents of the stator

v_{an}, v_{bn}, and v_{cn} are the phase to neutral voltages applied the stator

L_s is the self inductance of each of the three stator coils

R is the resistance of each of the three stator coils

M is the mutual inductance between each pair of the three stator coils

ϕ_a, ϕ_b, and ϕ_c are the flux linkages created by the PMs

and

$$\begin{bmatrix} \phi_a \\ \phi_b \\ \phi_c \end{bmatrix} = \begin{bmatrix} \phi_m \cos(n_p \theta_r) \\ \phi_m \cos(n_p \theta_r - \dfrac{2\pi}{3}) \\ \phi_m \cos(n_p \theta_r - \dfrac{4\pi}{3}) \end{bmatrix} \qquad (3.1)$$

where

ϕ_m represents the amplitude of the flux linkages produced by the PMs

θ_r is the mechanical angular position of the rotor, as defined below

n_p is the number of pole pairs

The reference for the angular position of the rotor is typically chosen to be the angle at which the center of an outward facing north pole of a PM aligns with the center of a phase a winding, while the winding is conducting a positive DC current. Additionally, phases b and c must be in parallel while conducting a negative DC current to provide balanced flux linkages. Note that if $n_p\theta_r$ equals zero in (3.1), ϕ_a equals ϕ_m, indicating a maximum magnet flux through winding a. More details concerning rotor position can be found in section 3.3.

The equivalent circuit of the non-salient PMSM model incorporates the series resistance and inductance of each phase. An electrical coupling exists between the phases and is depicted as a mutual inductance. This coupling is essentially constant in a non-salient PMSM, yet it varies in a salient PMSM and is easier to portray in the d-q frame of reference. There is also a back-EMF voltage equal to $\dfrac{d\phi}{dt}$, which opposes the voltage source. Evaluating the derivative of (3.1) leads to the back-EMF voltages

$$\begin{bmatrix} \dfrac{d\phi_a}{dt} \\ \dfrac{d\phi_b}{dt} \\ \dfrac{d\phi_c}{dt} \end{bmatrix} = -\begin{bmatrix} n_p\omega_r\phi_m\sin(n_p\theta_r) \\ n_p\omega_r\phi_m\sin(n_p\theta_r - \dfrac{2\pi}{3}) \\ n_p\omega_r\phi_m\sin(n_p\theta_r - \dfrac{4\pi}{3}) \end{bmatrix} \qquad (3.2)$$

32

and
$$\omega_r = \frac{d\theta_r}{dt} , \qquad (3.3)$$

$$\theta_e = n_p \theta_r , \qquad (3.4)$$

$$\omega_e = n_p \omega_r , \qquad (3.5)$$

where

ω_r is the mechanical speed of the rotor in radians per second,

ω_e is the electrical speed of the rotor in radians per second,

θ_e is the electrical angular position of the rotor in radians.

Assuming balanced conditions, there is no potential difference between points N_s and N_m in Figure 3.1. Applying Kirchoff's voltage law to phase a of Figure 3.1 gives

$$v_{an} = i_a R + L_s \frac{di_a}{dt} - M \frac{di_b}{dt} - M \frac{di_c}{dt} + \frac{d\phi_a}{dt} . \qquad (3.6)$$

To simplify (3.6), let $L = L_s + M$, and thus, $L_s = L - M$, to obtain

$$v_{an} = i_a R + L \frac{di_a}{dt} - M \left(\frac{di_a}{dt} + \frac{di_b}{dt} + \frac{di_c}{dt} \right) + \frac{d\phi_a}{dt} . \qquad (3.7)$$

Again, it is assumed that the system is balanced and therefore $i_a + i_b + i_c = 0$. Applying this assumption and (3.2) to (3.7) provides

$$v_{an} = i_a R + L \frac{di_a}{dt} - n_p \omega_r \phi_m \sin(n_p \theta_r) . \qquad (3.8)$$

The same procedure can be used to obtain the following equations for phases b and c:

$$v_{bn} = i_b R + L \frac{di_b}{dt} - n_p \omega_r \phi_m \sin(n_p \theta_r - \frac{2\pi}{3}) \qquad (3.9)$$

$$v_{cn} = i_c R + L \frac{di_c}{dt} - n_p \omega_r \phi_m \sin(n_p \theta_r - \frac{4\pi}{3}) \qquad (3.10)$$

In addition to (3.8), (3.9), and (3.10), the torque equation is needed to obtain the entire three-phase model of the non-salient PMSM. First, the electrical output power, $P_{e\text{-}out}$, of the motor is calculated by summing the back-EMF voltage and current product of each phase:

$$P_{e\text{-}out} = -i_a n_p \omega_r \phi_m \sin(n_p \theta_r) - i_b n_p \omega_r \phi_m \sin(n_p \theta_r - \frac{2\pi}{3}) - i_c n_p \omega_r \phi_m \sin(n_p \theta_r - \frac{4\pi}{3}). \quad (3.11)$$

The torque generated by the motor is obtained by dividing the electrical output power by the rotor speed, ω_r:

$$\tau_e = -i_a n_p \phi_m \sin(n_p \theta_r) - i_b n_p \phi_m \sin(n_p \theta_r - \frac{2\pi}{3}) - i_c n_p \phi_m \sin(n_p \theta_r - \frac{4\pi}{3}). \quad (3.12)$$

The entire torque equation is given by

$$J \frac{d\omega}{dt} = \tau_e - \tau_L, \quad (3.13)$$

or,

$$J \frac{d\omega}{dt} = -i_a n_p \phi_m \sin(n_p \theta_r) - i_b n_p \phi_m \sin(n_p \theta_r - \frac{2\pi}{3}) - i_c n_p \phi_m \sin(n_p \theta_r - \frac{4\pi}{3}) - \tau_L. \quad (3.14)$$

Thus, the entire non-salient PMSM model with $\theta_e = n_p \theta_r$ and $\omega_e = n_p \omega_r$ is

$$v_{an} = i_a R + L \frac{di_a}{dt} - \omega_e \phi_m \sin(\theta_e),$$

$$v_{bn} = i_b R + L \frac{di_b}{dt} - \omega_e \phi_m \sin(\theta_e - \frac{2\pi}{3}),$$

$$v_{cn} = i_c R + L \frac{di_c}{dt} - \omega_e \phi_m \sin(\theta_e - \frac{4\pi}{3}),$$

$$J \frac{d\omega}{dt} = -i_a n_p \phi_m \sin(\theta_e) - i_b n_p \phi_m \sin(\theta_e - \frac{2\pi}{3}) - i_c n_p \phi_m \sin(\theta_e - \frac{4\pi}{3}) - \tau_L.$$

$$(3.15)$$

3.3 The *d-q* Transformation

The *direct-quadrature* or *d-q* transformation converts a three-phase system with a stationary reference, such as the system given by 3.15, to an orthogonal two-phase system with a rotating reference. Not only is the model simplified due to the reduction of phases, but sinusoids are also eliminated due to the rotating reference. This transformation is most easily described as a two-step process. The first step, known as the Clarke transformation, consists of a three-phase to two-phase transformation that maintains a stationary reference and is defined by

$$
\begin{bmatrix} f_\alpha \\ f_\beta \\ f_0 \end{bmatrix} = \sqrt{\frac{2}{3}} \begin{bmatrix} 1 & -1/2 & -1/2 \\ 0 & \sqrt{3}/2 & -\sqrt{3}/2 \\ 1/\sqrt{2} & 1/\sqrt{2} & 1/\sqrt{2} \end{bmatrix} \begin{bmatrix} f_a \\ f_b \\ f_c \end{bmatrix}
\tag{3.16}
$$

where f_a, f_b, and f_c are the original three-phase vectors and f_α and f_β are the resulting two-phase vectors. These vectors may represent three-phase vectors such as i_a, i_b, i_c, and two-phase vectors i_α and i_β, with the transformation given by

$$
\begin{bmatrix} i_\alpha \\ i_\beta \\ i_0 \end{bmatrix} = \sqrt{\frac{2}{3}} \begin{bmatrix} 1 & -1/2 & -1/2 \\ 0 & \sqrt{3}/2 & -\sqrt{3}/2 \\ 1/\sqrt{2} & 1/\sqrt{2} & 1/\sqrt{2} \end{bmatrix} \begin{bmatrix} i_a \\ i_b \\ i_c \end{bmatrix}
\tag{3.17}
$$

In a balanced three-phase system, the zero component, i_0, equals zero. Thus, only two vectors are needed to describe a balanced three-phase system. The vector diagram in Figure 3.9 is a graphical portrayal of the transformation. Note that the vector f_α is in the same direction of f_a, and the orthogonal component, f_β, is 90 degrees apart from f_α.
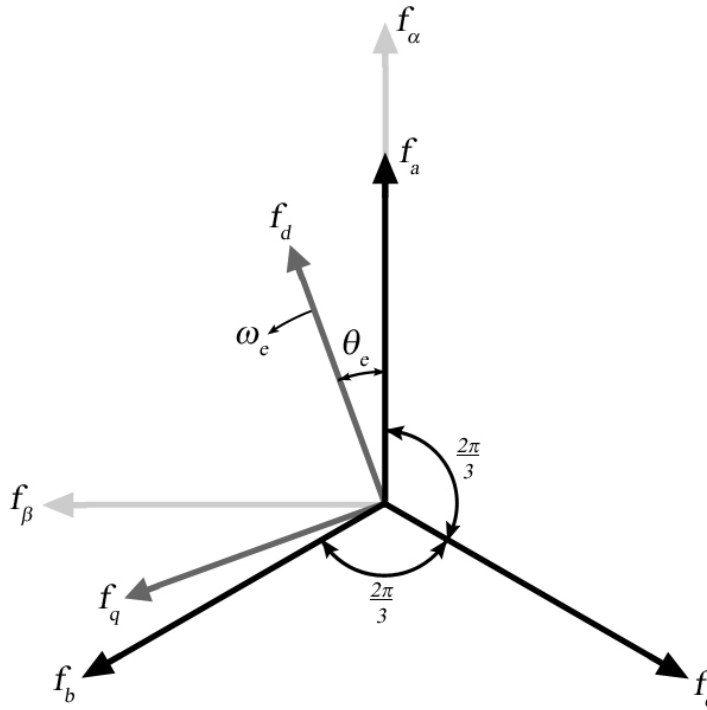
Figure 3.9. Vector diagram of *d-q* transformation

The second step of the *d-q* transformation, known as the Park transformation, converts the stationary reference two-phase vectors, f_α and f_β, to vectors with a rotating reference that are defined by

$$\begin{bmatrix} f_d \\ f_q \end{bmatrix} = \begin{bmatrix} \cos(\theta_e) & \sin(\theta_e) \\ -\sin(\theta_e) & \cos(\theta_e) \end{bmatrix} \begin{bmatrix} f_\alpha \\ f_\beta \end{bmatrix}$$

(3.18)

As shown in Figure 3.9, the *direct* and *quadrature* vectors, f_d and f_q respectively, are 90 degrees apart. The vector f_d lies upon the *direct* or *d-axis*, which is typically chosen to be aligned with the center of a PM with an outward facing north pole, as shown in Figure 3.10. The angle, θ_e, is defined to be the angle between the *d-axis* and the angle at which phase *a* produces a maximum flux, as described in section 3.2. Note that θ_e is not the three-phase phasor angle, which only affects the magnitude of the *d-q* components.

36
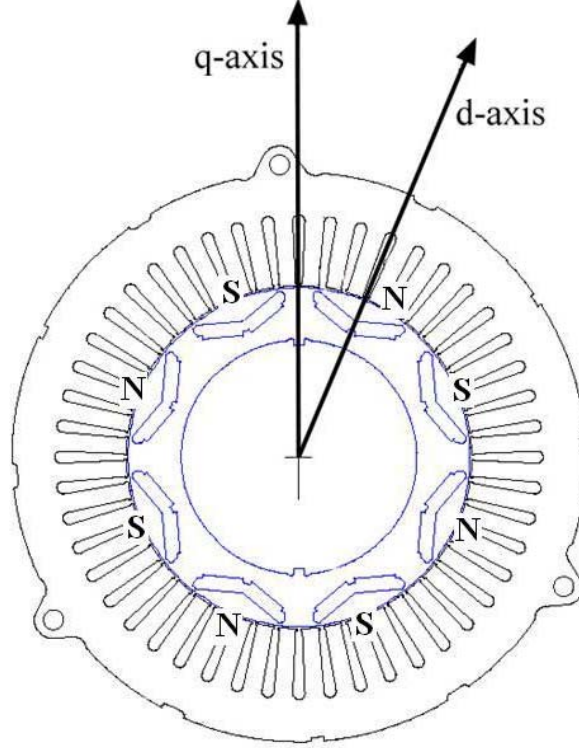
Figure 3.10. Direct axis alignment with Prius rotor

To directly obtain *d-q* vectors from the three-phase vectors, the Clarke and Park transforms can be combined to form the *d-q* transformation defined by

$$
\begin{bmatrix} f_d \\ f_q \\ f_0 \end{bmatrix} = \sqrt{\frac{2}{3}} \begin{bmatrix} \cos(\theta_e) & \cos(\theta_e - 2\pi/3) & \cos(\theta_e - 4\pi/3) \\ -\sin(\theta_e) & -\sin(\theta_e - 2\pi/3) & -\sin(\theta_e - 4\pi/3) \\ 1/\sqrt{2} & 1/\sqrt{2} & 1/\sqrt{2} \end{bmatrix} \begin{bmatrix} f_a \\ f_b \\ f_c \end{bmatrix} \qquad (3.19)
$$

Again, the zero component, f_0 , equals zero if the three-phase system is balanced. Therefore, assuming balanced conditions, the current transformation can be written as

$$
\begin{bmatrix} i_d \\ i_q \end{bmatrix} = \sqrt{\frac{2}{3}} \begin{bmatrix} \cos(\theta_e) & \cos(\theta_e - 2\pi/3) & \cos(\theta_e - 4\pi/3) \\ -\sin(\theta_e) & -\sin(\theta_e - 2\pi/3) & -\sin(\theta_e - 4\pi/3) \end{bmatrix} \begin{bmatrix} i_a \\ i_b \\ i_c \end{bmatrix} \qquad (3.20)
$$

and the voltage transformation is expressed by

$$\begin{bmatrix} v_d \\ v_q \end{bmatrix} = \sqrt{\frac{2}{3}} \begin{bmatrix} \cos(\theta_e) & \cos(\theta_e - 2\pi/3) & \cos(\theta_e - 4\pi/3) \\ -\sin(\theta_e) & -\sin(\theta_e - 2\pi/3) & -\sin(\theta_e - 4\pi/3) \end{bmatrix} \begin{bmatrix} v_a \\ v_b \\ v_c \end{bmatrix} \qquad (3.21)$$

Since the vectors in the *d-q* reference frame are somewhat arbitrary, there are several variations of the *d-q* transformation. In this case, the Park transformation was chosen so that the power remains the same:

$$P_{in} = v_a i_a + v_b i_b + v_c i_c = v_d i_d + v_q i_q \qquad (3.22)$$

Another transformation known as the Blondel transformation is similar to (3.19), but the $\sqrt{2/3}$ is replaced with 2/3 and the $1/\sqrt{2}$ with 1/2. With this transformation, as described in [10], the voltage and current magnitudes in the *d-q* frame, $\sqrt{f_d^2 + f_q^2}$, equals the phase voltage and current magnitude in the stationary frame.

The inverse *d-q* transformation is used to transform *d-q* vectors to three-phase vectors with a stationary reference. This transformation is often used in field-oriented control to translate *d-q* command signals to three-phase command signals for voltage or current control. The inverse *d-q* transformation is defined by

$$\begin{bmatrix} f_a \\ f_b \\ f_c \end{bmatrix} = \sqrt{\frac{2}{3}} \begin{bmatrix} \cos(\theta_e) & -\sin(\theta_e) & 1/\sqrt{2} \\ \cos(\theta_e - 2\pi/3) & -\sin(\theta_e - 2\pi/3) & 1/\sqrt{2} \\ \cos(\theta_e - 4\pi/3) & -\sin(\theta_e - 4\pi/3) & 1/\sqrt{2} \end{bmatrix} \begin{bmatrix} f_d \\ f_q \\ f_0 \end{bmatrix} \qquad (3.23)$$

If the three-phase vectors represent ideal sinusoids, with the system in steady state, the *d-q* vectors have a constant magnitude. Thus, the three-phase model given by (3.15) can be simplified to a two-phase model with *d-q* components that do not vary in steady state.

3.4 A *d-q* Model of the Non-Salient PM Machine

The three-phase model of the non-salient PM machine given by (3.15) will now be converted to the *d-q* reference frame, or synchronous frame. For simplicity, the transformation will be applied term by term. Thus, using (3.20) and (3.21), the phase equations in (3.15) are transformed to be

$$v_d = i_d R + L y_d - e_d \tag{3.24}$$

$$v_q = i_q R + L y_q - e_q \tag{3.25}$$

where

e_d and e_q are the transformed *d-q* vectors of the back-EMF terms

y_d and y_q are the transformed *d-q* vectors of di_a/dt, di_b/dt, and di_c/dt

According to (3.15) and (3.19), e_d and e_q can be defined by

$$\begin{bmatrix} e_d \\ e_q \end{bmatrix} = \sqrt{\frac{2}{3}} \begin{bmatrix} \cos(\theta_e) & \cos(\theta_e - 2\pi/3) & \cos(\theta_e - 4\pi/3) \\ -\sin(\theta_e) & -\sin(\theta_e - 2\pi/3) & -\sin(\theta_e - 4\pi/3) \end{bmatrix} \begin{bmatrix} \omega_e \phi_m \sin(\theta_e) \\ \omega_e \phi_m \sin(\theta_e - \frac{2\pi}{3}) \\ \omega_e \phi_m \sin(\theta_e - \frac{4\pi}{3}) \end{bmatrix} \tag{3.26}$$

Evaluating e_d and e_q separately

$$e_d = \sqrt{\frac{2}{3}} \omega_e \phi_m \left(\sin(\theta_e)\cos(\theta_e) + \sin(\theta_e - \frac{2\pi}{3})\cos(\theta_e - \frac{2\pi}{3}) + \sin(\theta_e - \frac{4\pi}{3})\cos(\theta_e - \frac{4\pi}{3}) \right)$$

Eliminating sinusoids which sum to zero through 120-degree separation,

$$e_d = 0 \tag{3.27}$$

$$e_q = \sqrt{\frac{2}{3}} \omega_e \phi_m \left(-\sin^2(\theta_e) - \sin^2(\theta_e - \frac{2\pi}{3}) - \sin^2(\theta_e - \frac{4\pi}{3}) \right)$$

And since $\sin^2(\theta_e) + \sin^2(\theta_e + 2\pi/3) + \sin^2(\theta_e + 4\pi/3) = 3/2$,

$$e_q = -\sqrt{\frac{2}{3} \frac{3}{2}} \omega_e \phi_m = -\sqrt{\frac{3}{2}} \omega_e \phi_m \qquad (3.28)$$

Notice that the back-EMF term is only present in the *q-axis* equation. This is an important benefit that provides a straightforward approach to flux weakening and is discussed later. Now, expressions for y_d and y_q will be determined. First, the phase currents must be expressed in terms of i_d and i_q. According to (3.23), with $i_0 = 0$,

$$i_a = \sqrt{2/3} \left(i_d \cos(\theta_e) - i_q \sin(\theta_e) \right) \qquad (3.29)$$

Evaluating the derivative of the current in phase *a*

$$\frac{di_a}{dt} = \frac{d}{dt} \left(\sqrt{2/3} \left(i_d \cos(\theta_e) - i_q \sin(\theta_e) \right) \right)$$

$$\frac{di_a}{dt} = \sqrt{\frac{2}{3}} \left(\frac{di_d}{dt} \cos(\theta_e) - i_d \omega_e \sin(\theta_e) - \frac{di_q}{dt} \sin(\theta_e) - i_q \omega_e \cos(\theta_e) \right) \qquad (3.30)$$

Using the same approach, the current derivatives for phases *b* and *c* are

$$\frac{di_b}{dt} = \sqrt{\frac{2}{3}} \left(\frac{di_d}{dt} \cos(\theta_e - \frac{2\pi}{3}) - i_d \omega_e \sin(\theta_e - \frac{2\pi}{3}) - \frac{di_q}{dt} \sin(\theta_e - \frac{2\pi}{3}) - i_q \omega_e \cos(\theta_e - \frac{2\pi}{3}) \right) \quad (3.31)$$

$$\frac{di_c}{dt} = \sqrt{\frac{2}{3}} \left(\frac{di_d}{dt} \cos(\theta_e - \frac{4\pi}{3}) - i_d \omega_e \sin(\theta_e - \frac{4\pi}{3}) - \frac{di_q}{dt} \sin(\theta_e - \frac{4\pi}{3}) - i_q \omega_e \cos(\theta_e - \frac{4\pi}{3}) \right) \quad (3.32)$$

Now, the current derivatives can be used in the following expression for y_d and y_q, obtained using (3.19):

$$\begin{bmatrix} y_d \\ y_q \end{bmatrix} = \sqrt{\frac{2}{3}} \begin{bmatrix} \cos(\theta_e) & \cos(\theta_e - 2\pi/3) & \cos(\theta_e - 4\pi/3) \\ -\sin(\theta_e) & -\sin(\theta_e - 2\pi/3) & -\sin(\theta_e - 4\pi/3) \end{bmatrix} \begin{bmatrix} di_a/dt \\ di_b/dt \\ di_c/dt \end{bmatrix} \qquad (3.33)$$

Evaluating y_d,

$$\begin{aligned}
y_d = \sqrt{\frac{2}{3}} \Bigg(&\sqrt{\frac{2}{3}} \left(\frac{di_d}{dt} \cos^2(\theta_e) - i_d \omega_e \sin(\theta_e) \cos(\theta_e) \right. \\
&\left. - \frac{di_q}{dt} \sin(\theta_e) \cos(\theta_e) - i_q \omega \cos^2(\theta_e) \right) \\
+ &\sqrt{\frac{2}{3}} \left(\frac{di_d}{dt} \cos^2(\theta_e - \frac{2\pi}{3}) - i_d \omega_e \sin(\theta_e - \frac{2\pi}{3}) \cos(\theta_e - \frac{2\pi}{3}) \right. \\
&\left. - \frac{di_q}{dt} \sin(\theta_e - \frac{2\pi}{3}) \cos(\theta_e - \frac{2\pi}{3}) - i_q \omega_e \cos^2(\theta_e - \frac{2\pi}{3}) \right) \\
+ &\sqrt{\frac{2}{3}} \left(\frac{di_d}{dt} \cos^2(\theta_e - \frac{4\pi}{3}) - i_d \omega_e \sin(\theta_e - \frac{4\pi}{3}) \cos(\theta_e - \frac{4\pi}{3}) \right. \\
&\left. - \frac{di_q}{dt} \sin(\theta_e - \frac{4\pi}{3}) \cos(\theta_e - \frac{4\pi}{3}) - i_q \omega_e \cos^2(\theta_e - \frac{4\pi}{3}) \right) \Bigg)
\end{aligned}$$

Eliminating sinusoids which sum to zero through 120-degree separation,

$$\begin{aligned}
y_d = \frac{2}{3} \Bigg(&\left(\frac{di_d}{dt} \cos^2(\theta_e) - i_q \omega_e \cos^2(\theta_e) \right) \\
+ &\left(\frac{di_d}{dt} \cos^2(\theta_e - \frac{2\pi}{3}) - i_q \omega_e \cos^2(\theta_e - \frac{2\pi}{3}) \right) \\
+ &\left(\frac{di_d}{dt} \cos^2(\theta_e - \frac{4\pi}{3}) - i_q \omega_e \cos^2(\theta_e - \frac{4\pi}{3}) \right) \Bigg)
\end{aligned}$$

41

Since $\cos^2(\theta_e) + \cos^2(\theta_e + 2\pi/3) + \cos^2(\theta_e + 4\pi/3) = 3/2$, y_d can be expressed by

$$y_d = \frac{di_d}{dt} - i_q \omega_e \tag{3.34}$$

Using the same approach, an expression for y_q is found:

$$
\begin{aligned}
y_q = \sqrt{\frac{2}{3}}\Bigg(&\sqrt{\frac{2}{3}}\Big(-\frac{di_d}{dt}\cos(\theta_e)\sin(\theta_e) + i_d\omega_e \sin^2(\theta_e) \\
&\qquad + \frac{di_q}{dt}\sin^2(\theta_e) + i_q\omega_e \cos(\theta_e)\sin(\theta_e) \Big) \\
+ &\sqrt{\frac{2}{3}}\Big(-\frac{di_d}{dt}\cos(\theta_e - \frac{2\pi}{3})\sin(\theta_e - \frac{2\pi}{3}) + i_d\omega_e \sin^2(\theta_e - \frac{2\pi}{3}) \\
&\qquad + \frac{di_q}{dt}\sin^2(\theta_e - \frac{2\pi}{3}) + i_q\omega_e \cos(\theta_e - \frac{2\pi}{3})\sin(\theta_e - \frac{2\pi}{3}) \Big) \\
+ &\sqrt{\frac{2}{3}}\Big(-\frac{di_d}{dt}\cos(\theta_e - \frac{4\pi}{3})\sin(\theta_e - \frac{4\pi}{3}) + i_d\omega_e \sin^2(\theta_e - \frac{4\pi}{3}) \\
&\qquad + \frac{di_q}{dt}\sin^2(\theta_e - \frac{2\pi}{3}) + i_q\omega_e \cos(\theta_e - \frac{2\pi}{3})\sin(\theta_e - \frac{2\pi}{3}) \Big)
\end{aligned}
$$

After cancellation of sinusoids,

$$
\begin{aligned}
y_q = \frac{2}{3}\Bigg(&\Big(i_d\omega_e \sin^2(\theta_e) + \frac{di_q}{dt}\sin^2(\theta_e) \Big) \\
+ &\Big(i_d\omega_e \sin^2(\theta_e - \frac{2\pi}{3}) + \frac{di_q}{dt}\sin^2(\theta_e - \frac{2\pi}{3}) \Big) \\
+ &\Big(i_d\omega_e \sin^2(\theta_e - \frac{4\pi}{3}) + \frac{di_q}{dt}\sin^2(\theta_e - \frac{4\pi}{3}) \Big) \Bigg)
\end{aligned}
$$

Since $\sin^2(\theta_e) + \sin^2(\theta_e + 2\pi/3) + \sin^2(\theta_e + 4\pi/3) = 3/2$,

$$y_q = i_d \omega_e + \frac{di_q}{dt} \tag{3.35}$$

42

The voltage equations for the non-salient IPM machine in the *d-q* frame are found by substituting e_d , e_q , y_d , and y_q from (3.27), (3.28), (3.34), and (3.35) into (3.24) and (3.25),

$$v_d = i_d R + L\frac{di_d}{dt} - L i_q \omega_e \tag{3.36}$$

$$v_q = i_q R + L\frac{di_q}{dt} + L i_d \omega_e + \sqrt{\frac{3}{2}}\omega_e \phi_m \tag{3.37}$$

To obtain the torque equation in terms of *d-q* variables, the input power to the motor is found by using (3.22). Thus, if (3.36) is multiplied by i_d and (3.37) is multiplied by i_q, the sum of the results will yield the input power:

$$P_{in} = v_d i_d + v_q i_q = i_d^2 R + L i_d \frac{di_d}{dt} - L i_d i_q \omega_e + i_q^2 R + L i_q \frac{di_q}{dt} + L i_d i_q \omega_e + \sqrt{\frac{3}{2}}\omega_e \phi_m i_q$$

Collecting and canceling terms in addition to assuming no power dissipation is involved with energy storage of the inductor,

$$P_{in} = \left(i_d^2 + i_q^2\right)R + \sqrt{\frac{3}{2}}\omega_e \phi_m i_q \tag{3.38}$$

It is clear that the first term is the power dissipated as heat in the windings, and the output power of the motor can be expressed by

$$P_{out} = \sqrt{\frac{3}{2}}\omega_e \phi_m i_q = \sqrt{\frac{3}{2}}n_p \omega_m \phi_m i_q \tag{3.39}$$

Dividing by ω_m reveals the generated torque, and thus the torque equation is defined by

$$J\frac{d\omega}{dt} = \sqrt{\frac{3}{2}}n_p \phi_m i_q - \tau_L \tag{3.40}$$

3.5 A *d-q* Model of the Salient PM Machine

The salient PM machine model is very similar to the non-salient PM machine model, yet there is a very important distinction between the two. As discussed in section 3.1, interior permanent magnet (IPM) machines allow for the flux created by the stator currents to pass through the rotor without passing through PM material. Saliency occurs when the permeability varies considerably around the circumference of the rotor. The size, location, and orientation of the PM material affect the salient behavior. For example, the permeance varies significantly between the *d* and *q axes* for the design shown in Figure 3.11 [11]. In fact, the saliency of this design creates the opportunity for extra torque to be produced in addition to the PM torque.
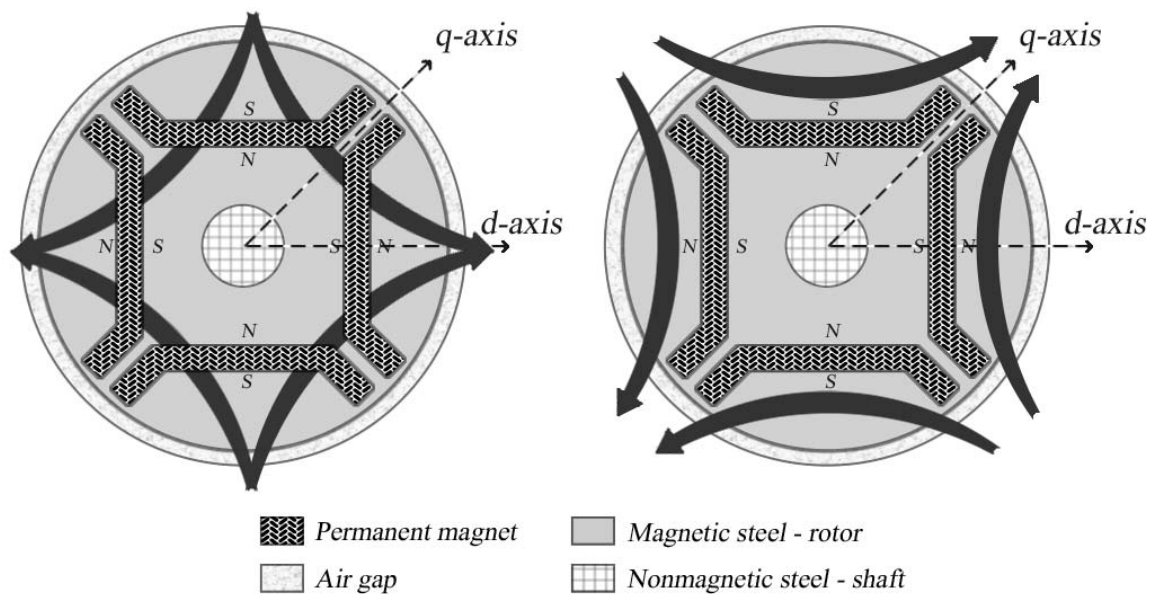
Figure 3.11. IPM machine saliency [11]

Since the permeance of the salient PM machine varies with rotor position, the model is most easily portrayed in the *d-q* synchronous frame. Similar to the design shown in Figure 3.11, IPM machines are typically designed to have a higher permeability along the *q-axis*, when compared to the permeability along the *d-axis*. Thus, the corresponding *q-axis* inductance, L_q, is greater than the *d-axis* inductance, L_d. This is different from the non-salient PM machine, where the *q-axis* and *d-axis* inductances are approximately equal. Consequently, the *d-q* equations for the non-salient PM machine given by (3.36) and (3.37) can be modified to obtain the *d-q* equations for the salient PM machine. This is done by simply replacing L with L_d or L_q in the following manner:

$$v_d = i_d R + L_d \frac{di_d}{dt} - L_q i_q \omega_e \tag{3.41}$$

$$v_q = i_q R + L_q \frac{di_q}{dt} + L_d i_d \omega_e + \sqrt{\frac{3}{2}} \omega_e \phi_m \tag{3.42}$$

The terms $-L_q i_q \omega_e$ and $+L_d i_d \omega_e$ in (3.41) and (3.42) are the voltages induced by mutual coupling between the *d* and *q* axes. The most significant difference is seen in the torque equation. First, similar to the non-salient model, the power will first be determined by multiplying (3.41) and (3.42) by i_d and i_q respectively, and summing the result:

$$P_{in} = \left(i_d^2 + i_q^2\right)R + L_d i_d \frac{di_d}{dt} - L_q i_d i_q \omega_e + L_q i_q \frac{di_q}{dt} + L_d i_d i_q \omega_e + \sqrt{\frac{3}{2}} \omega_e \phi_m i_q \tag{3.43}$$

Collecting terms and assuming $L_d\, i_d \dfrac{di_d}{dt}$ and $L_q\, i_q \dfrac{di_q}{dt}$ are negligible, and thus no power dissipation is involved with energy storage of the inductor,

$$P_{in} = \left(i_d^{\,2} + i_q^{\,2}\right)R + (L_d - L_q)\,i_d i_q \omega_e + \sqrt{\frac{3}{2}}\,\omega_e \phi_m i_q \tag{3.44}$$

Subtracting the I^2R losses, the output power is given by

$$P_{out} = (L_d - L_q)\,i_d i_q \omega_e + \sqrt{\frac{3}{2}}\,\omega_e \phi_m i_q \tag{3.45}$$

Dividing by $\omega_m = \omega_e / n_p$ gives the generated torque and the torque equation is expressed by

$$J\frac{d\omega}{dt} = n_p (L_d - L_q)\,i_d i_q + \sqrt{\frac{3}{2}}\,n_p \phi_m i_q - \tau_L \tag{3.46}$$

Rearranging (3.41) and (3.42) leads to the standard state-space model of the salient PM machine in the d-q reference frame with $\theta_e = n_p \theta_r$ and $\omega_e = n_p \omega_r$ is

$$L_d \frac{di_d}{dt} = v_d - i_d R + L_q\, i_q n_p \omega_m \tag{3.47}$$

$$L_q \frac{di_q}{dt} = v_q - i_q R - L_d i_d n_p \omega_m - K n_p \omega_m \tag{3.48}$$

$$J\frac{d\omega_m}{dt} = n_p (L_d - L_q)\,i_d i_q + n_p K i_q - \tau_L \tag{3.49}$$

$$\frac{d\theta_m}{dt} = \omega_m \tag{3.50}$$

where $K = \sqrt{\dfrac{3}{2}}\,\phi_m$ is the two phase equivalent of the torque and back-EMF constant.

Notice the torque term in (3.49) that is proportional to $L_d - L_q$. In the non-salient PM machine, this term is negligible since L_d and L_q are approximately equal. In the motoring operation region, torque is produced with i_q being positive and n_p is always a positive constant. If the IPM machine is designed such that L_q is greater than L_d, then the difference, $L_d - L_q$, is negative. Therefore, a negative i_d will make the term, $n_p(L_d - L_q)\, i_d i_q$, positive and more torque is produced in addition to the torque created by the PMs. This additional torque is referred to as reluctance torque.

Several benefits are gained from having the reluctance torque component. Firstly, more torque can be attained with the same current limit, or for the same rated torque, the maximum current can be reduced. In the latter case, cooling system requirements are not as challenging since the motor operates at lower currents, and thus lower temperatures. Since a smaller amount of current is needed to produce the same amount of torque, salient PM machines can achieve higher efficiencies than PM machines. Additionally, less PM material is needed to produce the same amount of torque. Thus, with a lower amount of PM flux, the machine can be operated at higher speeds due to the reduction of induced back-EMF voltage. Furthermore, the manufacturing costs of the motor are decreased if smaller magnets are used.

The magnet size, location, and orientation influence the achievable efficiency, torque, power, and speed range of the PM machine. The relationship between magnet parameters and performance characteristics are very complex, and finite element analysis is necessary for a detailed study, such as in [10] and [12].

3.6 Field Oriented Control of the Salient PM Machine

Several methods can be used to control a PM machine. Typically, current feedback is used to regulate control signals to a voltage source inverter (VSI). Although attempts have been made to generalize sensorless control of PM machines, as described in [13], position feedback is normally used since precise rotor position is needed to optimally control the machine. It is desirable to eliminate the position sensor to reduce volume and manufacturing costs, yet the unpredictable conditions and load transients of a vehicular system present a substantial barricade, particularly for near zero speeds.

On a fundamental level, vehicles are inherently torque controlled, where the torque command is produced by the accelerator pedal on traditional vehicles. For HEVs, the torque command to the motor is based on the accelerator pedal, but it is also affected by other parameters such as the state of charge (SOC) of the battery back. Controllers for PM machines often include speed feedback to address flux-weakening requirements. Closed loop speed feedback control is also used in some applications, such as the implementation discussed hereafter.

Regardless of the control scheme used, PM machines require flux weakening at high speeds due to the induced back-EMF voltage, which has an amplitude that increases with speed. According to (2.1), the absolute maximum RMS phase voltage available from a PWM controlled VFI is $0.45V_{dc}$. For stability purposes, the inverter is often operated in the linear region below the over-modulation region and the corresponding maximum voltage is even smaller. At a particular speed, the back-EMF voltage exceeds

the voltage available from the VSI, and without flux-weakening or phase advance control methods, this is the maximum operating speed of the motor with no load. Under these conditions, no load can be applied because there is no voltage available to force a torque producing current through the windings. For rotor speeds below this speed and above base speed, this phenomenon limits the torque producing capability of the machine.

Various control methods are used to suppress limitations imposed by the induced back-EMF voltage. The conventional phase advance (CPA) control method uses a transistor firing scheme to apply voltage to the stator windings during instances where the back-EMF voltage is lower than the voltage available from the VSI. However, the motor must be designed with a high inductance to avoid excessively high currents for the wide constant power speed range (CPSR) needed in automotive applications. This large inductance is unappealing in terms of volume and manufacturing cost. A technique presented in [14] and [15], called dual-mode inverter control (DMIC), uses thyristors between the VSI and the motor terminals to prevent current flow through the bypass diodes. This eliminates an associated braking component, and reduces the current requirement for a given torque. Additionally, the current-minimizing inductance is much lower than that of the CPA control method. The most significant drawback to this method is the cost of the additional thyristors, which can be offset by reduced motor size and cooling system requirements.

A flux-weakening control method presented in this thesis uses a current to produce a flux that opposes the PM flux, and therefore reduces the back-EMF voltage. The *d-q* synchronous frame is well suited for this control method, as the *d-axis* is aligned with the direction of the magnetic field of a PM. The associated PM flux is an area-based

49

quantity, and the normal to this flux surface is aligned with the *d-axis*. Thus, the PM flux is often described to be along the *d-axis*, yet this statement is not entirely accurate, as flux has no direction. The term "field weakening" is also inaccurate since the magnetic field is not weakened, under normal operation [9]. Thus, a vector, $\vec{\phi}_{pm}$, is defined to have a magnitude equal to $\sqrt{3/2}\phi_m$, the two-phase equivalent PM flux linkage, and a direction along the normal to the flux surface, which is aligned with the center of the north pole of a PM. Although contradictive, this and similar vectors will be referred to as flux vectors.

The concept of flux weakening is similar between SPM and IPM machines, yet the control method is quite different due to the presence of reluctance torque in IPM machines. Henceforth, development will be focused on control of IPM machines, as the Toyota Prius is an IPM machine. To simplify the development, it will be assumed that the rotor speed, ω_m, and the applied load, τ_L, is constant. Applying these assumptions to (3.47), (3.48), and (3.49) provides the steady-state equations

$$v_d = i_d R - L_q \, i_q n_p \omega_m \tag{3.51}$$

$$v_q = i_q R + L_d i_d n_p \omega_m + K n_p \omega_m \tag{3.52}$$

$$\tau_L = n_p (L_d - L_q) \, i_d i_q + n_p K i_q \tag{3.53}$$

with the voltage and current constraints defined by

$$V = \sqrt{{v_d}^2 + {v_q}^2} \leq V_{max} = \sqrt{\frac{3}{2}} \, v_{max} \tag{3.54}$$

$$I = \sqrt{{i_d}^2 + {i_q}^2} \leq I_{max} = \sqrt{\frac{3}{2}} \, i_{max} \tag{3.55}$$

50

where v_{max} is the maximum peak phase voltage given by (2.1) times $\sqrt{2}$

i_{max} is the maximum peak current per phase.

The current limitation, i_{max}, is typically determined by several characteristics which include the type of insulation used on the windings and the heat transfer capability of the motor and cooling system. The voltage limitation, v_{max}, is determined by the output voltage of the battery pack or the boost converter if it present.

The behavior of the model and the impact of these limitations are well portrayed in graphical form. Following the approach and color scheme similar to that of Otuday, et.al. in [12], a vector diagram of the IPM machine described by (3.51) and (3.52), without flux weakening, and thus with $i_d = 0$, is shown in Figure 3.12.
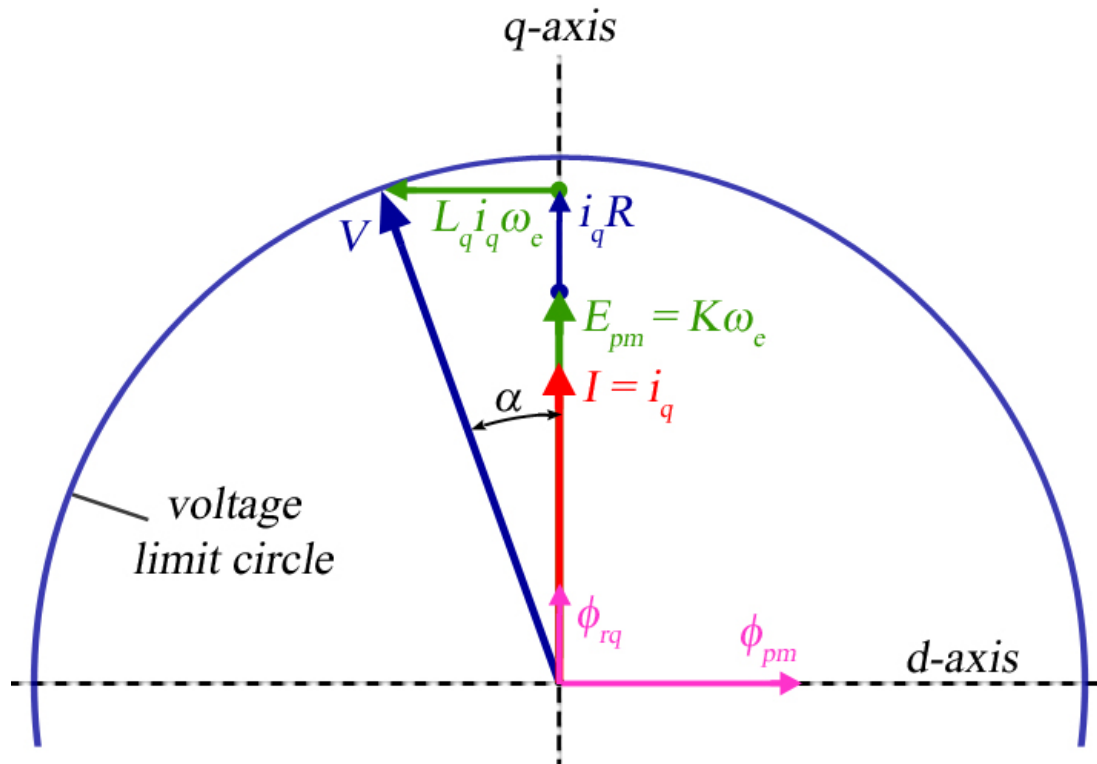

Figure 3.12. IPM machine vector diagram without flux weakening

where

α is the angle between the terminal voltage and stator current vectors

δ represents the angle between the stator current vector and the *q-axis*

$\phi_{rq} = L_q i_q$ is the flux vector magnitude due to the *q-axis* current

$\phi_{rd} = L_d i_d$ is the flux vector magnitude due to the *d-axis* current

E_{pm} is the two-phase, *d-q* equivalent of the back-EMF voltage

Note that the quantities shown on the diagram and discussed below are vector magnitudes of the two-phase *d-q* equivalents of the three phase quantities. The back-EMF voltage, E_{pm}, resistive voltage drop, $i_q R$, and reaction flux, ϕ_{rq}, are always aligned with the *q-axis*. The PM flux vector magnitude, ϕ_{pm}, and the reaction flux, ϕ_{rd}, are aligned with the *d-axis*. Without flux-weakening, the reaction flux, ϕ_{rd}, is not present since i_d equals zero. The voltage vector, *V*, is composed of the *d-q* components v_d and v_q. The diagram in Figure 3.12 portrays a particular case in which the voltage equals the voltage limit that is depicted by the blue circle. If the rotor speed increases and the load remains constant, the magnitude of both voltage components must increase, and thus the voltage restraint is violated. Therefore, a negative *d-axis* current is used to create a reaction flux, ϕ_{rd}, which opposes the PM flux and effectively reduces the induced back-EMF voltage as shown in Figure 3.13. The associated *q-axis* voltage reduction has a magnitude of $L_d i_d \omega_e$. An additional *d-axis* resistive voltage drop also appears, as i_d is non-zero. Without flux weakening, the voltage vector represented by the faded blue vector extends beyond the voltage limit circle.
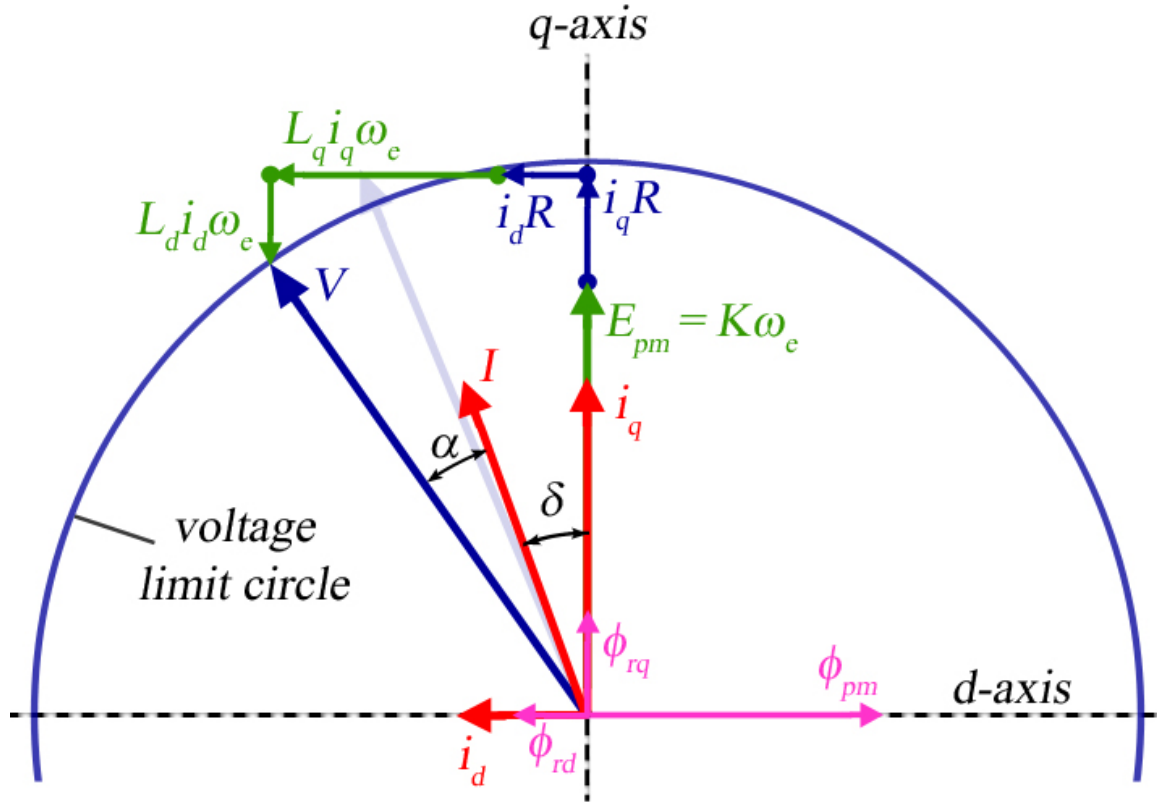
Figure 3.13. IPM machine vector diagram with flux weakening and increased speed

By applying a negative d-axis current at high speeds, the required voltage can be reduced below the voltage limit. As the amplitude of this current is increased, the current vector rotates counter-clockwise, and α typically decreases. Similarly, the voltage vector rotates counter-clockwise and δ increases as v_d increases and v_q decreases. An infinite amount of voltage and current vector combinations exist that will cause the IPM machine to operate at a particular torque and speed. An optimal voltage and current vector combination exists that will maximize the efficiency of the motor, and this combination does not typically correspond to a unity power factor. There are complex tradeoffs involved in deciphering the optimal amount of field weakening and reluctance torque.

In SPM machines, the flux weakening current, i_d, is held at zero until the motor reaches a speed and torque when the back-EMF overwhelms the supply voltage. If the motor is producing maximum torque, flux weakening begins to be required at base speed. Beyond this speed, the maximum torque capability decreases as the required amount of flux weakening current increases. Therefore, with increasing speed, the input power increases through I^2R losses, although the output power remains constant. However, IPM machines have a benefit over SPM machines through reluctance torque. As the flux weakening current, i_d, increases, the reluctance torque in (3.53) is increased in addition to having a reduced back-EMF. Thus, the input power and output power of the IPM machine increases as the flux weakening current increases.

As opposed to SPM machines, optimal control of IPM machines consists of applying a negative *d-axis* current below base speed to develop reluctance torque. This complicates the designation of the optimal field-weakening current to be used for a particular torque and speed. Consequently, an accurate model of the machine is necessary unless the reference values are chosen empirically. Additionally, current and voltage limitations greatly influence the manner in which the motor is optimally controlled. An exemplar diagram with a current limit circle and voltage limit ellipses is shown in Figure 3.14 [16]. A voltage limit ellipse exists for each speed, and portrays the possible i_d and i_q currents associated with a given maximum voltage, according to (3.51), (3.52), and (3.54). Note that this ellipse represents the voltage limit in terms of the current, and would be a fixed sized circle if it were plotted in terms of voltage.
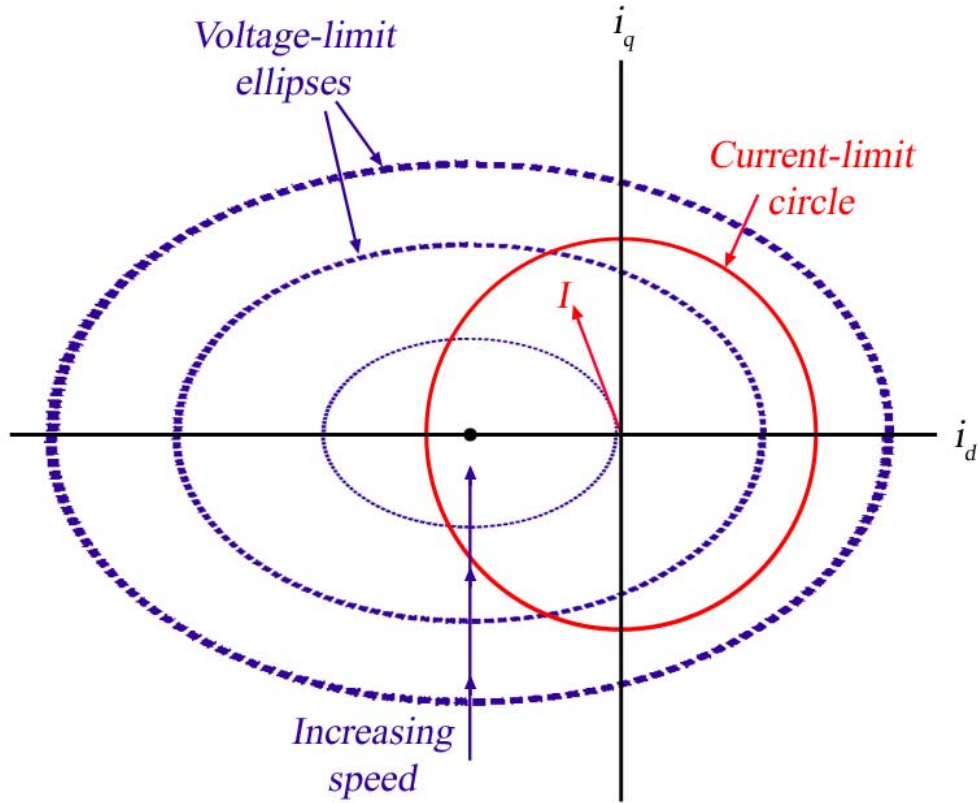
Figure 3.14. SPM machine current and voltage limits [16]

Since the minimum flux weakening current amplitude increases with speed, the corresponding minimum voltage amplitude, $|v_d|$, increases as well. To remain within the voltage limit, the *q-axis* voltage must satisfy $v_q \leq \sqrt{V_{max}^2 - v_d^2}$.

An understanding of optimal flux weakening will be conveyed by following an approach similar to that of [16]. The more straightforward control of the SPM machine will be described to establish a basis before moving to the IPM machine. Similar to Figure 3.14, a graph of the current and voltage limits for the SPM machine is shown in Figure 3.15.

55

Figure 3.15. SPM machine current and voltage limits with current trajectories
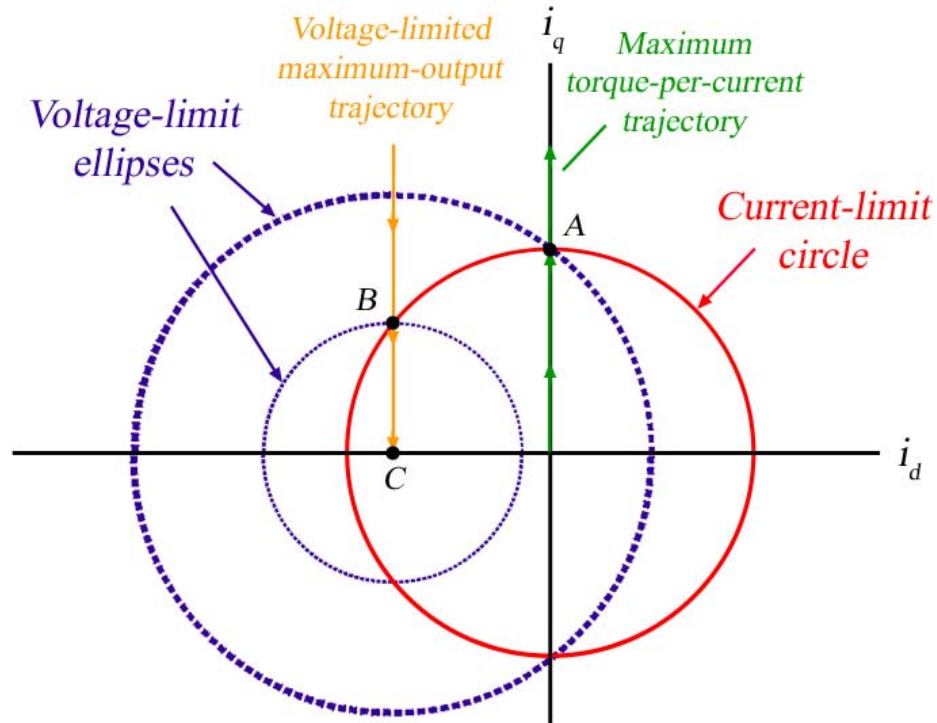
A maximum torque-per-amp trajectory for the SPM is shown for an ideal case where there is no voltage limit. In this case, all current vectors are aligned with the *q-axis*. Also shown is a voltage limited maximum-output trajectory that does not consider current constraints. Below base speed, the optimal current vector increases from the origin to point *A* as torque increases. With current and voltage constraints considered, the optimal current vector for maximum torque stays at point *A*, where $i_d = 0$, until base speed is reached. As the speed increases beyond base speed, the current vector follows the current limit circle to point *B*. Then, the current vector follows the voltage-limited trajectory to point *C,* where the maximum speed is reached. A similar graph for the IPM machine is shown in Figure 3.16.
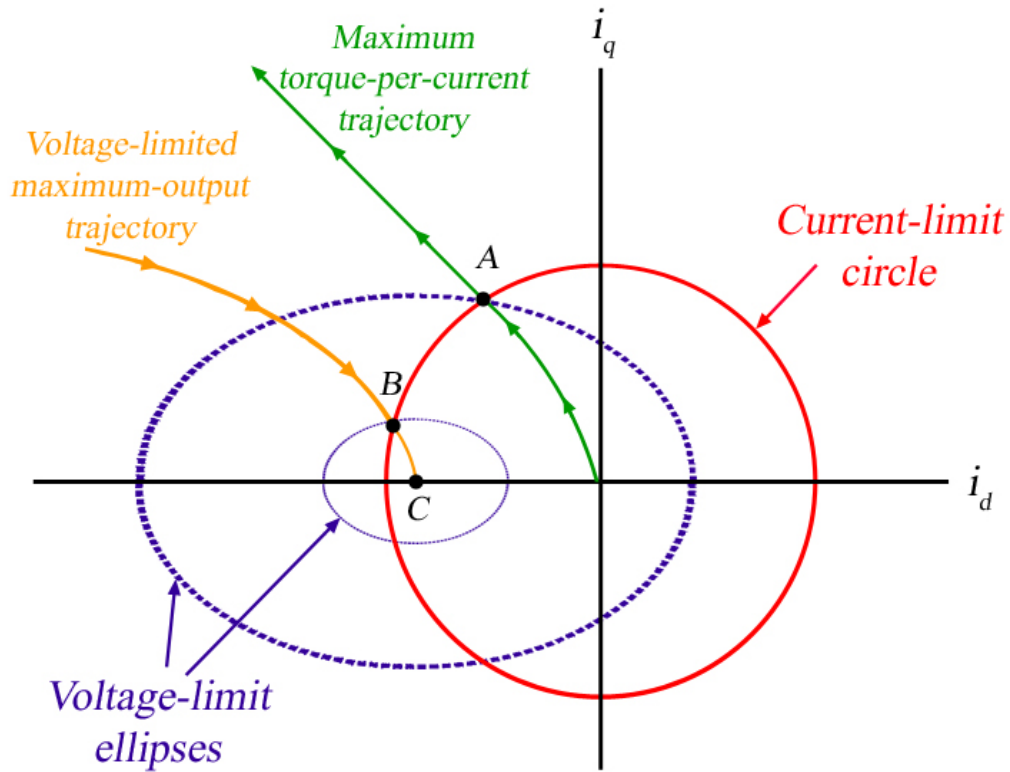
Figure 3.16. IPM machine current and voltage limits with current trajectories

The maximum torque-per-amp trajectory without voltage limitations is no longer along the *q-axis* since it is more efficient to partially use reluctance torque from a negative *d-axis* current. The optimal voltage-limited trajectory without current limitations also reflects this phenomenon. Below base speed, the optimal current vector increases from the origin to point *A* as torque increases. With current and voltage constraints considered, the optimal current vector for maximum torque stays at point *A* until base speed is reached. As the speed increases beyond base speed, the current vector follows the current limit circle to point *B*. Then, the current vector follows the voltage-limited trajectory to point *C,* where the maximum speed is reached.

In the cases present above, the highest operation speed at point *C*, corresponds

with a *d-axis* current equal to $-\dfrac{K}{L_d} = -\sqrt{\dfrac{3}{2}}\dfrac{\phi_m}{L_d}$. For a wide speed range and reasonable

operation limits, PM machines should be designed such that $-K/L_d$ is close to I_{max} [16].

Otherwise, if $-K/L_d$ is much less than I_{max}, then the speed range will be limited. If $-K/L_d$

is much larger than I_{max}, then the required current and voltage will be large. In this case,

the optimal maximum torque current trajectory would follow the current limit circle until

it reaches the *d-axis*.

It has been shown that obtaining just the maximum torque current trajectory may

be difficult, especially if the exact motor model, current limitation, and voltage limitation

is not known. The evaluation presented in Chapter 4 involves a thorough test that covers

the entire torque-speed range of the 2004 Prius motor. Thus, the tests entail a wide range

of optimal current trajectories and since the exact motor parameters, harmonic influences,

and saturation effects were not known, an empirical approach was taken to determine the

optimal current trajectories.

3.7 Summary

The various categories of PM machines have been presented along with neglections and assumptions that significantly reduce the complexity of the PM machine models. A three-phase, stationary frame model of the SPM machine was developed and the *d-q* transformation was presented and applied to obtain the *d-q* equivalent model of the SPM machine. Then, the cause and effects of saliency were presented as the IPM machine was modeled in the *d-q* synchronous frame. Using this model, steady-state conditions were assumed to simplify the perception and development of a field-oriented control method. The general form of optimal current trajectories was presented in vector diagram format with current and voltage constraints in consideration. The implementation of this control method for the evaluation of the 2004 Prius is discussed in Chapter 4.

Chapter 4

Experimental Evaluation

4.1 Experimental Setup

The goal of the evaluation presented in this thesis is to study various characteristics of the 2004 Prius IPM machine over the entire torque-speed range. Although rough estimates of the motor parameters are easily obtained, these estimated values do not provide the accuracy needed to determine the optimal current trajectories if they are used in the motor model. Methods to obtain these parameters are discussed and their susceptibility to variance and impact of inaccuracy on the model is presented. Consideration of core losses, which are primarily due to eddy currents and hysteresis in the rotor laminations, are of great complexity and therefore are not part of this discussion.

If the machine is not accurately modeled, it is impossible to determine the most efficient current trajectory. Therefore, the optimal current trajectory was determined online in an empirical manner. A current-speed feedback controller was implemented to suit this approach. A real-time PC interface, Opal-RT, was used to develop the controller in a rapid and easily modifiable manner. The laboratory environment and equipment setup are described along with the most difficult obstacle to overcome, impacts of electromagnetic interference (EMI) on feedback and measurement signals. Therefore, some elementary concepts of the causes and countermeasures of EMI are discussed.

4.1.1 Parameter Identification and Impact of Ideal Assumptions

The easiest parameter to measure is the stator winding resistance. However, this resistance increases with increasing temperature, and can greatly affect the efficiency of the machine even for the same torque-speed operation point. Variance of the stator resistance will also affect the shape of optimal current trajectory. A resistance value can be obtained by simply measuring the resistance between two stator terminals, *a* and *b*, for example. Then the stator resistance is obtained by dividing by two since the resistance measurement is of two windings in series. To evaluate the variance of the resistance with temperature, several different resistance measurements can be made as the stator windings are at various temperatures. The resistances also increase due to the skin effect, in which high frequency signals associated high rotor speeds and inverter switching tend to travel on the outermost portion of a conductor.

Inductance measurements are not as straightforward as the resistance measurements since the inductance varies with rotor position and with saturation at high current levels. The inductance is closely related to permeance of the rotor, as described in section 3.4. The position of the rotor is typically defined to be the angular distance between the *d-axis* and angle at which a maximum air gap flux is obtained from a positive current through phase *a*, with phases *b* an *c* in parallel. Thus, the *d-axis* inductance, L_d, can be measured by holding the rotor fixed at the zero position and measuring the inductance between terminal *a*, and terminals *b* and *c* in parallel. Note that some prefer to define the rotor position with respect to the *q-axis* instead of the *d-axis*. The *q-axis* is 90 electrical degrees away from the *d-axis*, and L_q can be measured using

the same configuration, yet with the rotor fixed at 90 electrical degrees. Considering the impact of the parallel phases in series with phase *a*,

$$L_d = \frac{2}{3}L(0°) \tag{4.1}$$

$$L_q = \frac{2}{3}L(90°) \tag{4.2}$$

The *q-axis* inductance is typically larger than the *d-axis* inductance since the *d-axis* flux can travel through the rotor without passing through the PM. Therefore, at high currents, iron saturation occurs mostly on the *q-axis*, and L_q effectively decreases. This behavior creates a complex cross-coupling relationship between the two flux axes. Similarly, the torque and back-EMF factor, *K*, is also affected by iron saturation, yet details of these relationships are beyond the expanse of this thesis.

The approximate PM flux, ϕ_m, can be measured by using the back-EMF waveform voltage, or by using data from locked rotor tests. According to (3.8),

$$\phi_m = \frac{\sqrt{2}E_{rms}}{n_p\omega_m} \tag{4.3}$$

where E_{rms} is the RMS of the back-EMF phase voltage of any phase. The locked rotor test consists of feeding a DC current through phase *a*, with phases *b* and *c* in parallel and conducting a negative DC current. This is done with the rotor being prevented from moving, and thus a certain amount of torque is developed, depending on the rotor position. This test is performed over an electrical cycle for several different current levels to identify the torque characteristics of the machine. The approximate PM flux, ϕ_m, can be obtained by using (3.40). The torque obtained with the rotor positioned at 90

electrical degrees, corresponds to a current with $i_d = 0$ and $i_q = \sqrt{3/2}\,I_{DC}$. Thus, the

approximate PM flux is given by

$$\phi_m = \frac{2}{3}\frac{\tau_{PM}(90°)}{n_p I_{DC}}$$

(4.4)

where $\tau_L = \tau_{PM}$ since no reluctance torque is present. The graph in Figure 4.1 depicts the

separate contributions of PM torque and reluctance torque versus the current angle

according to (3.53), with $\delta = \tan^{-1}(-i_d/i_q)$. This reveals that the maximum torque per

current is obtained while neither PM torque nor reluctance torque is maximized. Note

that according to (4.4), ϕ_m appears to decrease as the stator flux begins to saturate at high

currents, effectively producing less torque per current. Since the relationship is non-

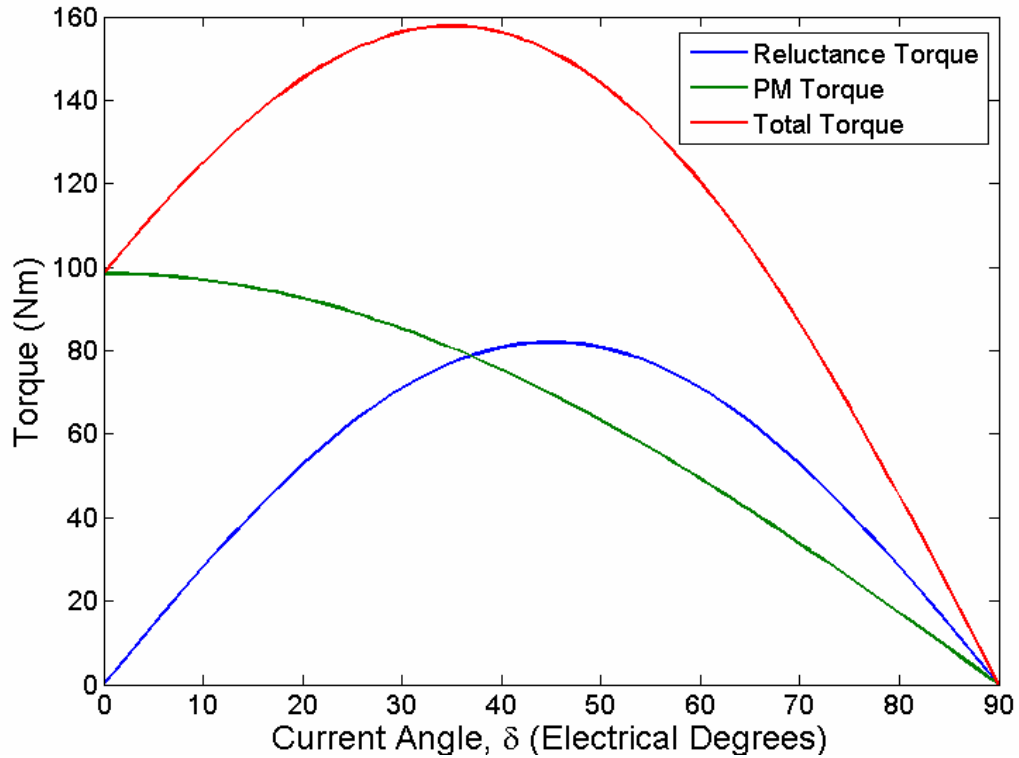linear, it is more accurate to define the PM torque in terms of a variable other than ϕ_m.

Figure 4.1. Reluctance torque, PM torque, and total torque

4.1.2 Controller Implementation

It has been shown that there is great difficulty in determining the optimal current trajectories for a wide range of speed and torques, especially with variance and saturation of the motor parameters. Since the 2004 Prius motor is regularly operated in high saturation regions, an online control method was used to determine the optimal current trajectories. A block diagram format of the control system is shown in Figure 4.2. A speed feedback loop is used to generate the *q-axis* reference current, which regulates the output torque of the motor to maintain the reference speed. The *d-axis* reference current is manually commanded, based on approximate trajectories made with the model given in Chapter 3. For each torque and speed, the *d-axis* current is varied in slight increments as the steady state efficiency of the motor is monitored. Thus, the optimal *d-axis* current can be obtained empirically.

Note that even if conditions for optimal motor operation are satisfied, optimal operation may not be obtained for both the motor and inverter combined. This pragmatic method of evaluation provides the opportunity to ensure that the entire system is operating most efficiently. In this experiment, it was found that although the inverter could be operated more efficiently, the conditions were such that the motor efficiency decreased and the entire system efficiency was essentially consistent.
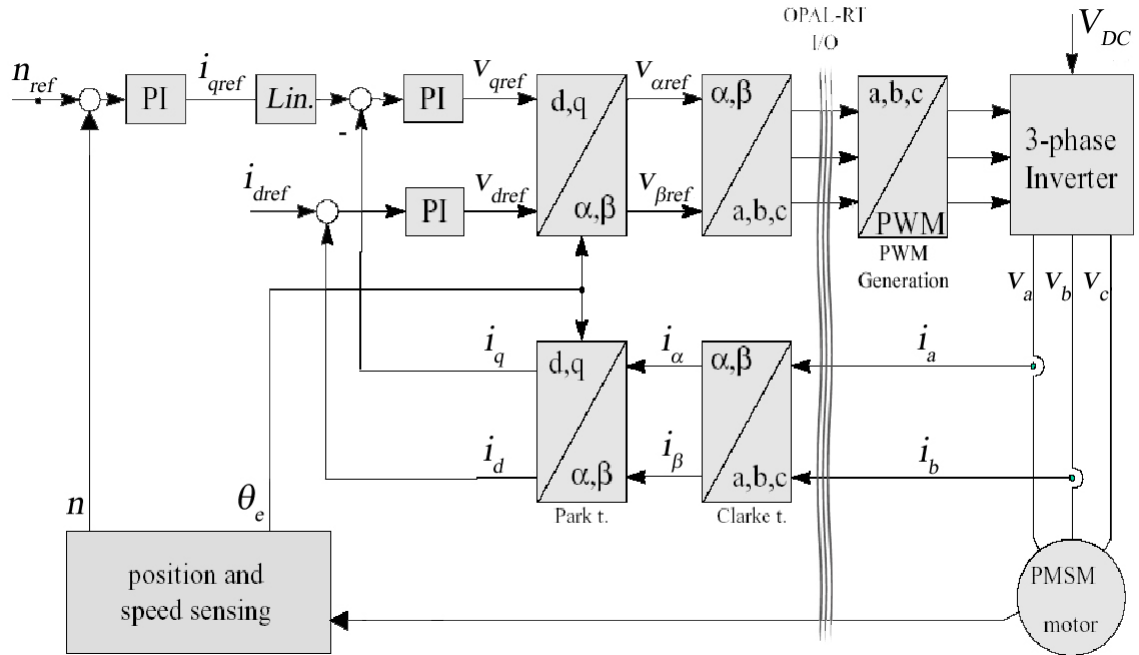
Figure 4.2. Current-speed feedback controller setup

The *d-q* currents are obtained by applying the *d-q* transformation to the three-phase currents, which are measured with only two current transducers since balanced conditions are assumed. The measured *q-axis* current is compared to the output of the standard proportional-integral (PI) speed controller, which is linearized according to (3.53). A comparison is also made between the measured *d-axis* current and a reference that is commanded directly. The *d-q* current errors are fed into two separate PI current controllers that generate the *d-q* voltage references. These *d-q* voltage references are then converted into three-phase entities through the inverse *d-q* transformation. A sine-triangular wave comparison technique is used to generate the PWM command signals for the 2004 Toyota Prius inverter and driver board, which incorporates dead-time generation to prevent shoot-through.

The controller was developed in block diagram format with Simulink. A real-time PC interface system, Opal-RT, was used to implement control algorithms and served as a console to provide system feedback and communication with the controller. A diagram of the system is shown is Figure 4.3. A console PC is used to build and modify the controller in Simulink. Then, the model is compiled and sent to the target nodes via an ethernet connection. These target nodes have dedicated operating systems and distribute the computational load of the control algorithms. A digital and analog interface with additional signal conditioning is used to receive feedback signals and transmit control signals to the inverter.
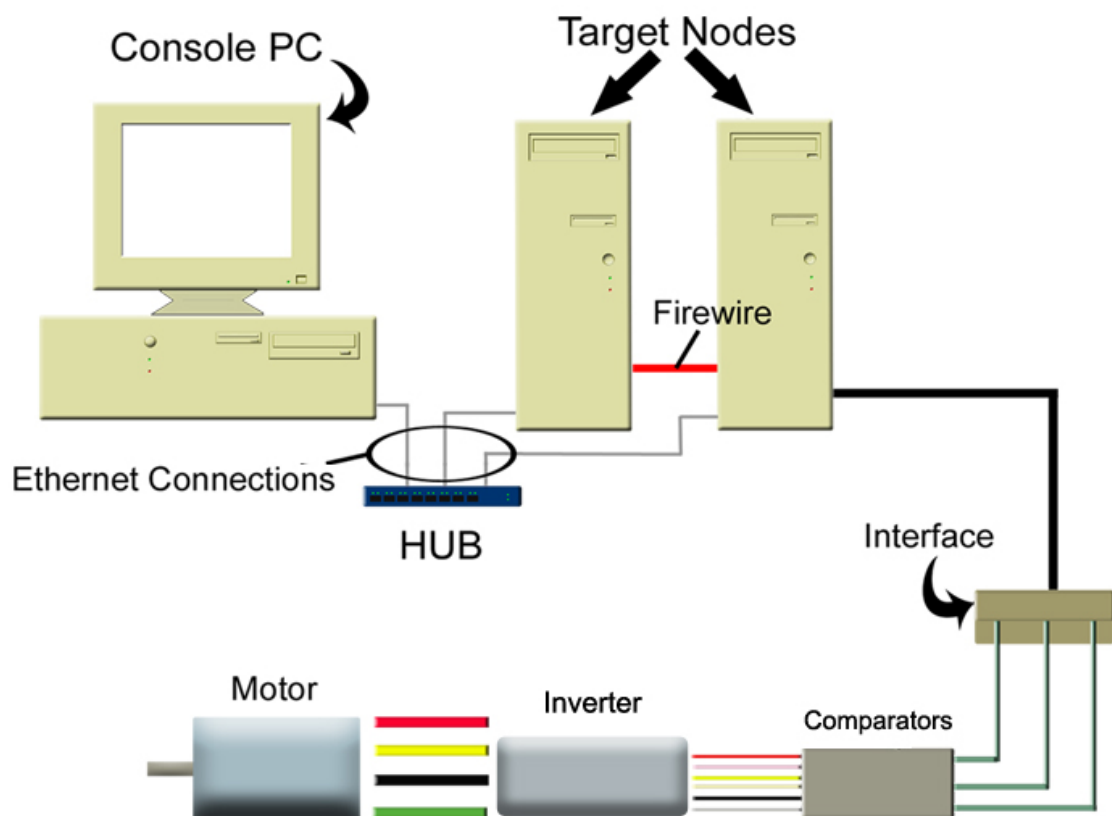

Figure 4.3. Real-time PC interface

Precise position feedback is needed to properly synchronize the stator field with the rotating field of the PMs. The 2004 Toyota Prius uses a Tamagawa Seiki Singlsyn resolver, which is an inductive type of position sensor with a quadrature output. When compared to an optical encoder, the inductive resolver has a lower cost and volume in addition to having a much higher speed range, which is important for future use. Furthermore, it provides accurate speed and position feedback necessary for control of PM machines.

Initially, an analytical approach was taken to obtain the proportional and integral gains for the current and speed controllers. However, since unexpected transients appeared in the feedback signals, a trial and error process was used to tune the gains. Although this led to a decrease in the controller gains, the system responsiveness remained well within the requirements of the evaluation. An investigation revealed that most of the unexpected transients were caused by EMI in the feedback cables to the controller.

Current transducers are used to scale the stator current feedback down to a level that the controller interface can withstand. The current is represented by a signal that is approximately 2000 times smaller than the original and thus a small amount of noise will appear to be a large current transient. There were also issues with EMI induced upon the speed and position feedback signals, which are originally analog signals, and are then converted to a multi-bit digital signal, both of which are susceptible to EMI. A significant amount of interference will prevent the controller from achieving stability, and may even cause the controller to become highly unstable.

67

4.1.3 Causes and Countermeasures of EMI

The high frequency switching of the inverter and boost converter causes sharp, high voltage transients. Similarly, abrupt changes occur in the radiated electromagnetic field surrounding the conductors carrying these transients. Thus, EMI may be induced in conductors carrying low-level signals in the proximity of these spurts of field strength.

Electromagnetic fields are radiated as current conducts through paths that are intended to exist and also through paths formed through stray capacitances or ground loops, which are usually not intended to exist. These currents are termed differential mode and common mode currents respectively. Similarly, a signal can be affected by EMI in two manners. Differential mode interference occurs when noise appears as a series component of a signal path. As an example, if a negative lead were routed through a strong electromagnetic field and the positive lead were not, noise would appear as a series component. When common mode interference occurs, both leads experience noise that is conducted through a ground loop. Thus, elimination of ground loops is extremely important to prevent EMI. Reduction of EMI is obtained by shielding and shortening high-level transient carrying conductors as well as low-level signal-carrying conductors. High-level and low-level conductors should have considerable separation between them, and if a crossing is necessary, the conductors should be oriented in a perpendicular manner. Filtering techniques can be used, but caution should be exercised to avoid signal degradations with increased rise and fall times.

4.1.4 Laboratory Setup

The 2004 Prius motor was evaluated at various torque and speeds in a dynamometer test cell at Oak Ridge National Laboratory. This type of evaluation provides the means to study the behavior and capabilities of the motor, such as peak and continuous performance in terms of thermal limitations or battery power. The dynamometer shown in Figure 4.4 [17] develops a braking torque caused by currents that are induced by a DC field current as the rotor rotates. The DC field current is adjusted to vary the amount of load applied to the motor. A speed sensor and torque transducer located between the dynamometer and the motor measures the rotor speed and amount of load applied to the motor. Due to the nature of this dynamometer, the low-speed torque capabilities do not match the Prius, and an additional PM motor and load bank was used to develop higher low-speed torques.
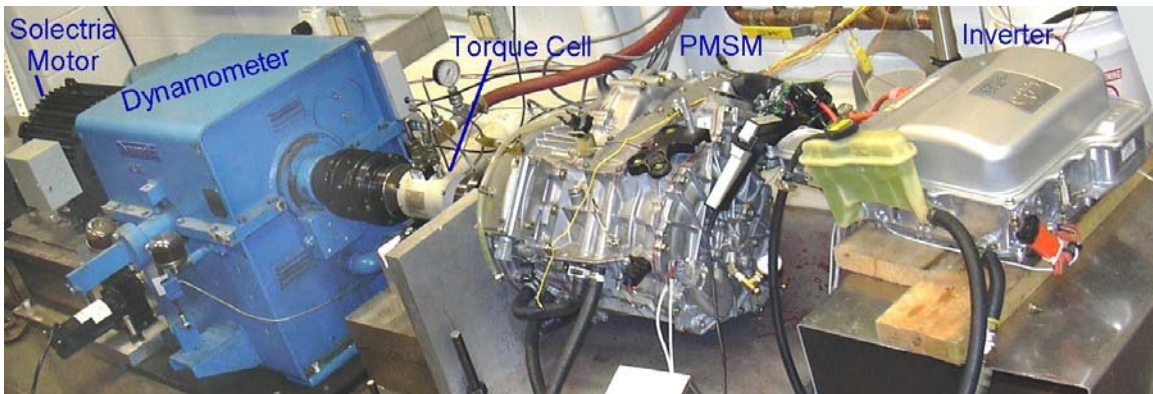

Figure 4.4. Dynamometer test cell [17]

A standard automotive ethylene-glycol coolant mixture was fed through the heat exchanger of the motor, which is in series with the inverter. Except for extremely high torque tests, the coolant was regulated at a temperature of 55 degrees Celsius with a flow rate of ~7 liters per minute. To study thermal characteristics and to ensure thermal limitations were not exceeded, thrermocouples were installed at various locations in the motor, as shown in Figure 4.5 [18]. These locations provide stator winding, oil, coolant, and internal/external case temperature measurements. The winding temperature of the Prius is limited to about 174 degrees Celsius. Oil is used to facilitate dissipation of heat generated by the windings through the motor casing and heat exchanger. Thermocouples were also installed in crevices between the inverter heat sink and heat exchanger.
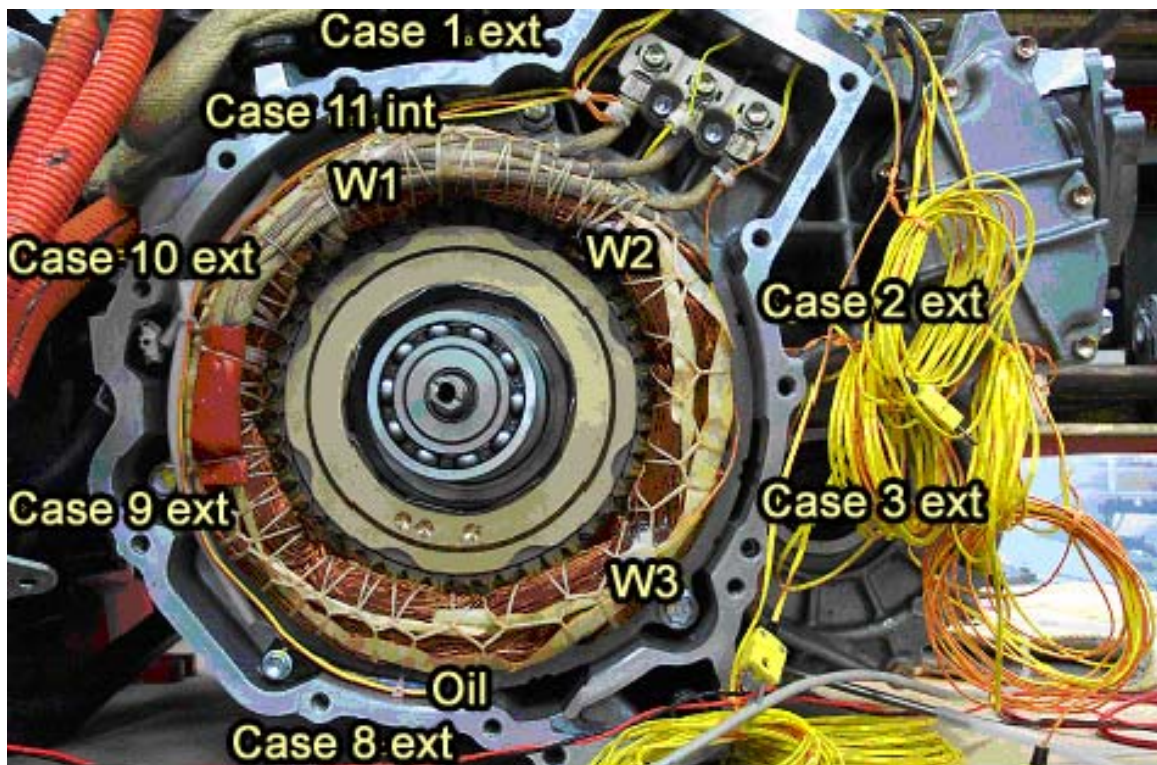

Figure 4.5. Thermocouple locations [18]

A data acquisition system was implemented by developing a visual basic program that communicates with several measurement instruments and consolidates data from these instruments in order to provide a convenient display of conditions such as current, temperature, power, efficiency, etc. The thermal data was obtained using a Keithly 2700 acquisition unit and the torque and speed data was gathered with a Himmelstein torque cell. The electrical measurements including current, voltage, and power were measured with a Yokogawa PZ4000 power analyzer.

A block diagram of the entire experiment setup is shown in Figure 4.6 [17]. Additional technical information and evaluations concerning the Prius Synergy drive that are not within the scope of this thesis can be found in [17].
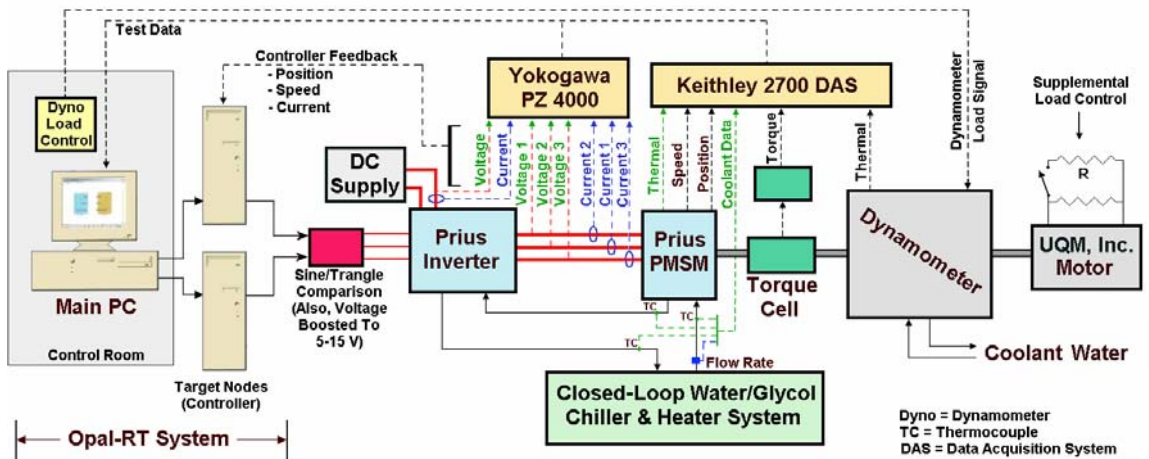

Figure 4.6. Entire system configuration [17]

4.2 Experimental Results

The model, control theory, and system configuration presented in Chapter 3 and section 4.1 was used to carry out performance tests on the 2004 Prius 50-kilowatt inverter and motor. The instantaneous torque and power capabilities of the motor are shown in Figures 2.3 and 2.4. The motor is claimed to have a power rating of 50 kilowatts, yet the battery pack and boost converter only have a power rating of about 20 kilowatts. Thus, for high power levels, the remaining power is obtained from the 30-kilowatt generator that is driven by the gasoline engine. In order to evaluate the motor and inverter over the entire operation range, the inverter was connected directly to a regulated DC supply and the boost converter was analyzed in a separate series of tests. An examination of the motor and application of the measurement methods presented in section 4.1 produced following motor parameters

$n_p = 4$ pole pairs

$L_d = 1.916$ mH $d\text{-}axis$ inductance

$L_q = 5$ mH $q\text{-}axis$ inductance (neglecting saturation)

$R = 0.065$ Ohms   winding resistance (at room temperature with DC current)

$K = 0.2$ Back-emf and torque-current factor (neglecting saturation)

$V_{max} = 390$ V   two-phase equivalent for maximum DC bus voltage of 500 V

$I_{max} = 380$ Amps   two-phase equivalent of 220 A RMS

4.2.1 Back-EMF Test Results

Back-EMF voltage measurements provide insight regarding the strength of the permanent magnets, as well as flux weakening requirements. The back-EMF voltage is measured as a secondary motor spins the subject motor with the three-phase motor leads disconnected from the inverter. If there is no external neutral available, a pseudo neutral can be created by connecting the leads to a balanced, high resistance Y load. The RMS phase voltage was measured over the entire speed range of the motor, and the results are shown in Figure 4.7. The voltage waveform and harmonic distribution of the back-EMF voltage is provided in Figures 3.2 and 3.4 of Chapter 3.
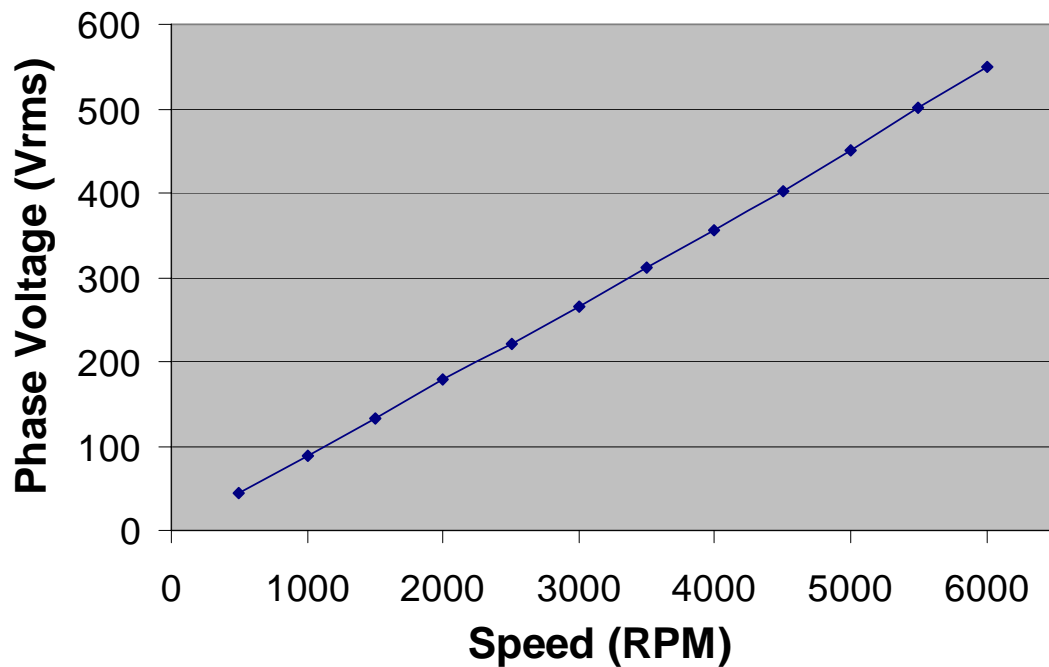

Figure 4.7. 2004 Prius back-EMF voltage meaurements

4.2.2 Locked Rotor Tests

The torque characteristics of a motor can be observed by conducting locked rotor tests, as described in section 4.1.1. A torque transducer is located between the motor and the locking mechanism. When DC current is applied to the stator windings, the associated stator flux attracts the PMs and torque is developed since the rotor is locked and the PMs are prevented from achieving a position of equilibrium. This procedure is performed at various current levels, as the rotor position is incremented through at least half of an electrical cycle. The torque over the entire cycle resembles a sinusoid, and has even or odd symmetry, depending on the reference position. The measured locked rotor torque for half of an electrical cycle is shown in Figure 4.8.
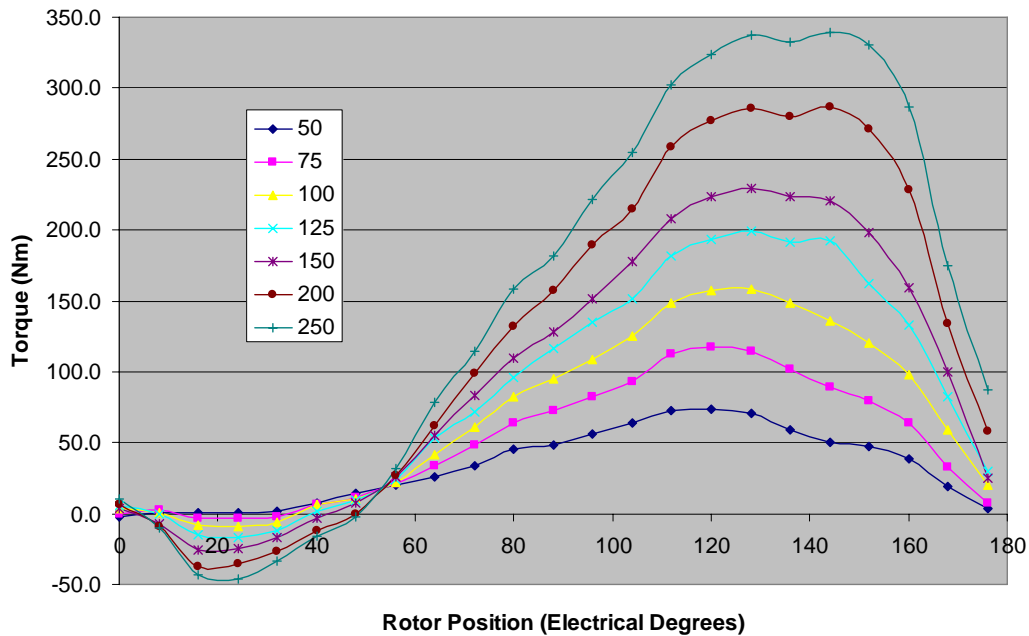

Figure 4.8. 2004 Prius locked rotor test results

According to Figure 4.8, the peak-torque for low currents occurs with a load angle of about 120 electrical degrees, or, $\alpha + \delta = 30^\circ$ in Figure 3.13. As the current increases, the peak-torque load angle also increases, and the effects of saturation begin to occur at a DC current of about 100 Amps. For very high currents, saturation is prominent and deformation is observed for rotor positions at which high torques are obtained. The measured peak-torque values for each current are shown in Figure 4.9. Also shown is the simulated locked rotor torque without saturation.
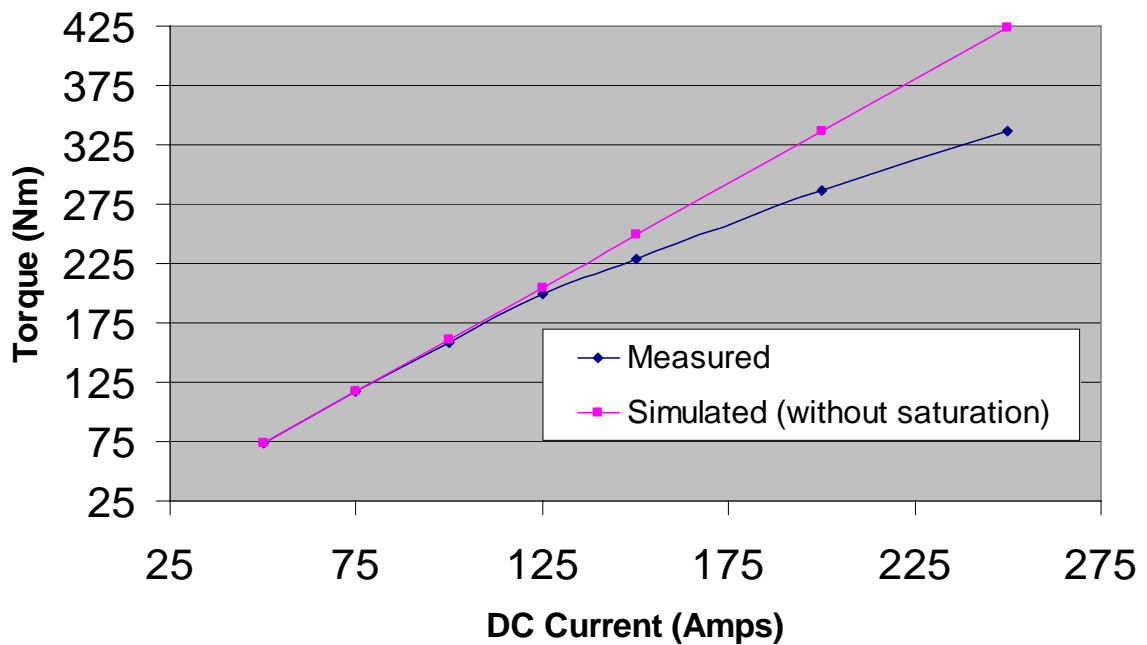

Figure 4.9. Peak locked rotor torque versus current

With a rated instantaneous torque of 400 Newton-meters, it is evident that the motor operates in saturation for a large portion of the entire operation region. The effects of saturation can be observed by calculating the torque-current factor, $K = \sqrt{\frac{3}{2}}\phi_m$, with ϕ_m defined by (4.4). The torque-current factor for each current is shown in Figure 4.10 and the values decrease drastically with increasingly high currents. These assessments are slightly lower than the value obtained using the back-EMF voltage and (4.3), where K = 0.214. The behavior and effects of iron saturation are difficult to predict and incorporate into the motor model. Thus, locked rotor tests provide useful information for verifying optimal torque per current operation of the controller, particularly for speeds below base speed.
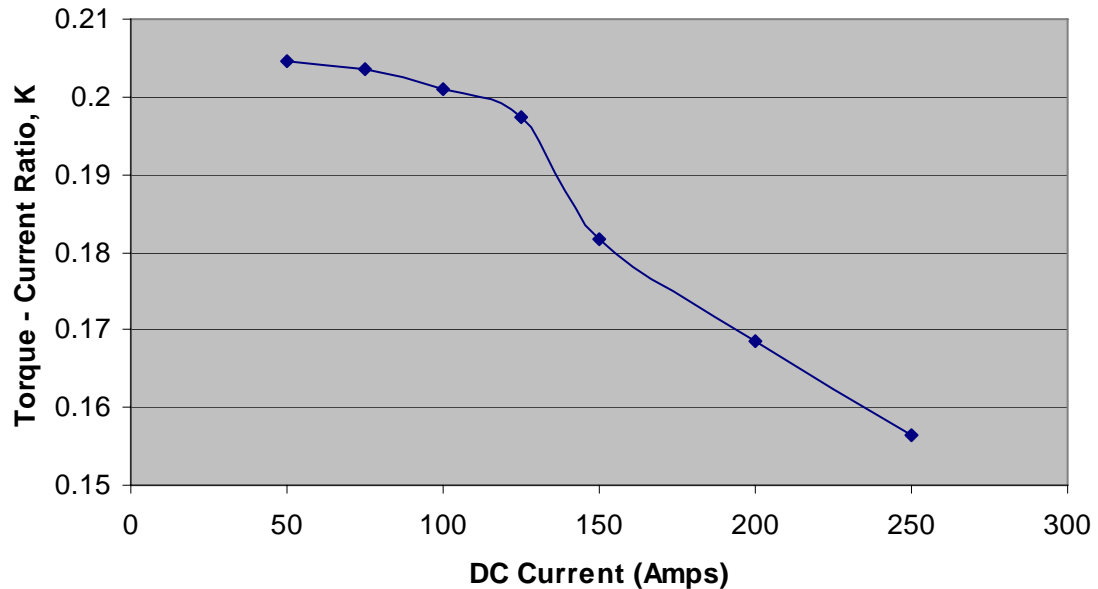
Figure 4.10. Peak locked rotor torque versus current

4.2.3 Boost Converter Efficiency Tests

The boost converter efficiency was evaluated at various currents and output voltages. The input DC voltage of the boost converter from the battery pack was measured to be between 200 and 250 Volts. Therefore, tests were performed with a consistent input DC voltage of about 233 V. A PWM signal is used to maintain the output voltage of the boost converter between 230 and 500 Volts, depending on driving conditions and state of charge. Filtering capacitors are located on both the low and high voltage side of the boost converter. The test results shown in Figure 4.11 were performed at several speeds to ensure data consistency.
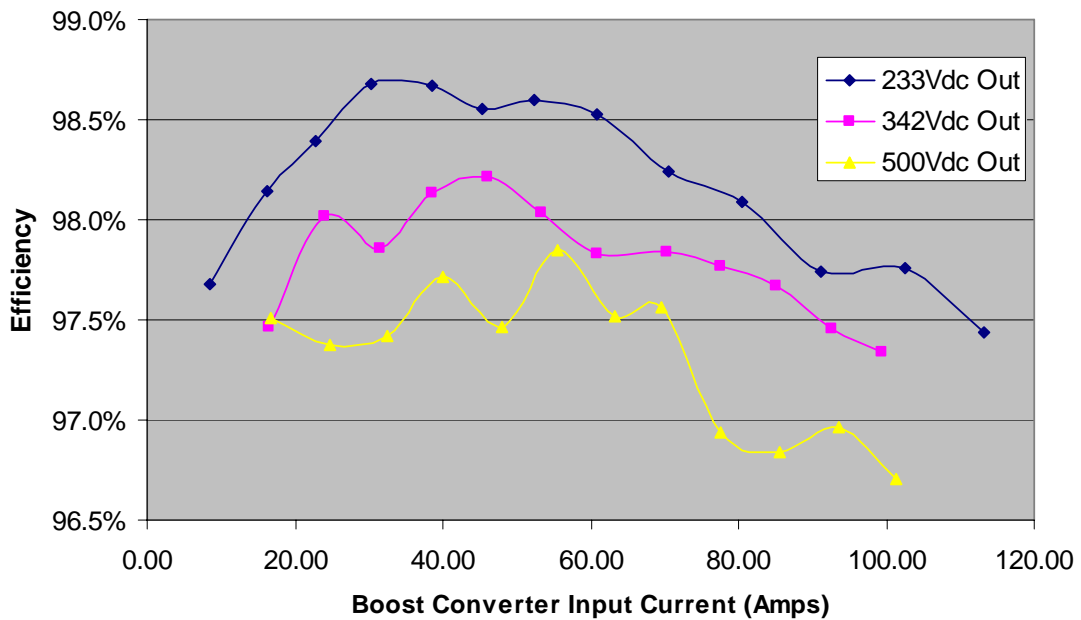

Figure 4.11. Boost converter efficiencies

4.2.4 Motor and Inverter Efficiency Mappings

The 2004 Prius 50-kilowatt inverter and motor were evaluated for most of the torque-speed range. For all data points, the motor was operated in steady state for at least 20 seconds to ensure data consistency. The data samples collected during this time were averaged to obtain the finalized data set. The motor efficiency is calculated by dividing the developed mechanical power by the AC input power to the motor. A three-dimensional graph is obtained when the efficiency is plotted for every torque and speed. A more indicative two-dimensional graph, shown in Figure 4.12, is generated by plotting the contours of the three-dimensional efficiency plot.
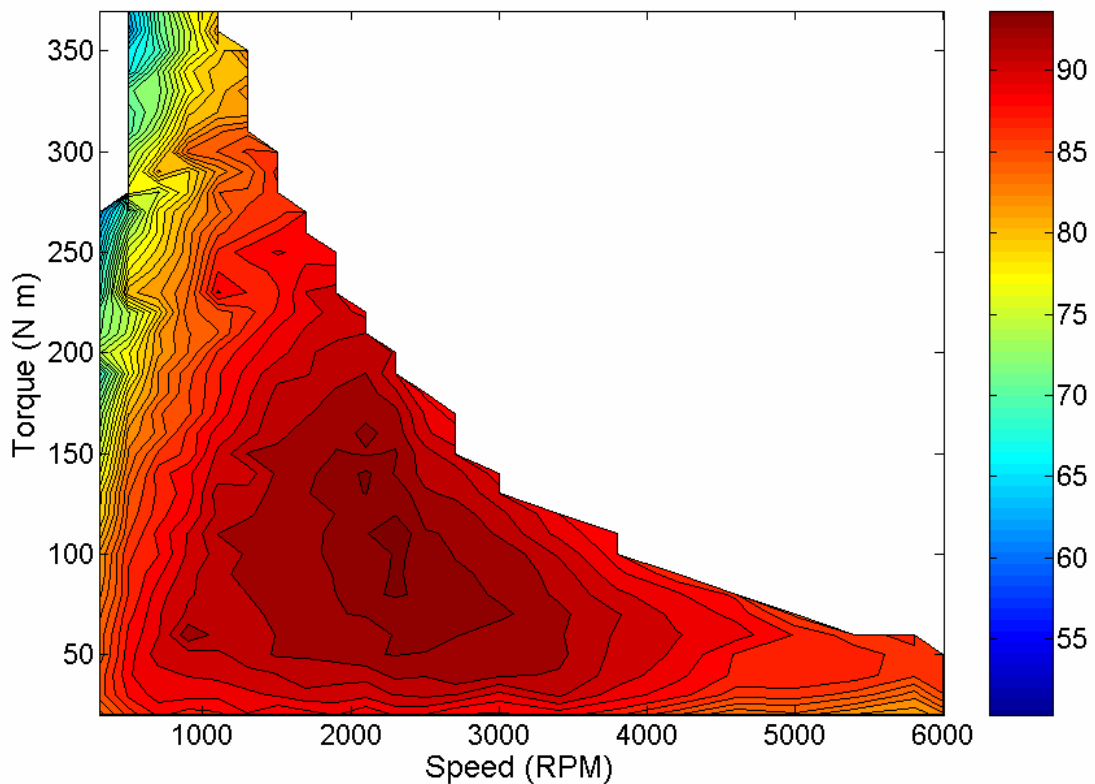
Figure 4.12. 2004 Prius motor efficiency contour map in one percent increments

The contours shown in Figure 4.12 were generated in one percent increments to reveal the gradient of the efficiency roll off, for all measured percentages. In order to generate the clearly labeled contour map shown in Figure 4.13, only efficiency contours greater than 70% were graphed and the increment of efficiency was increased for low efficiencies. Small contour islands were removed to eliminate confusion. It is shown that the motor efficiency surpasses 94%, and is above 90% for a large portion of the frequent driving regions described by Figure 2.2.

Figure 4.13. Motor efficiency contour map for efficiencies greater than 70%

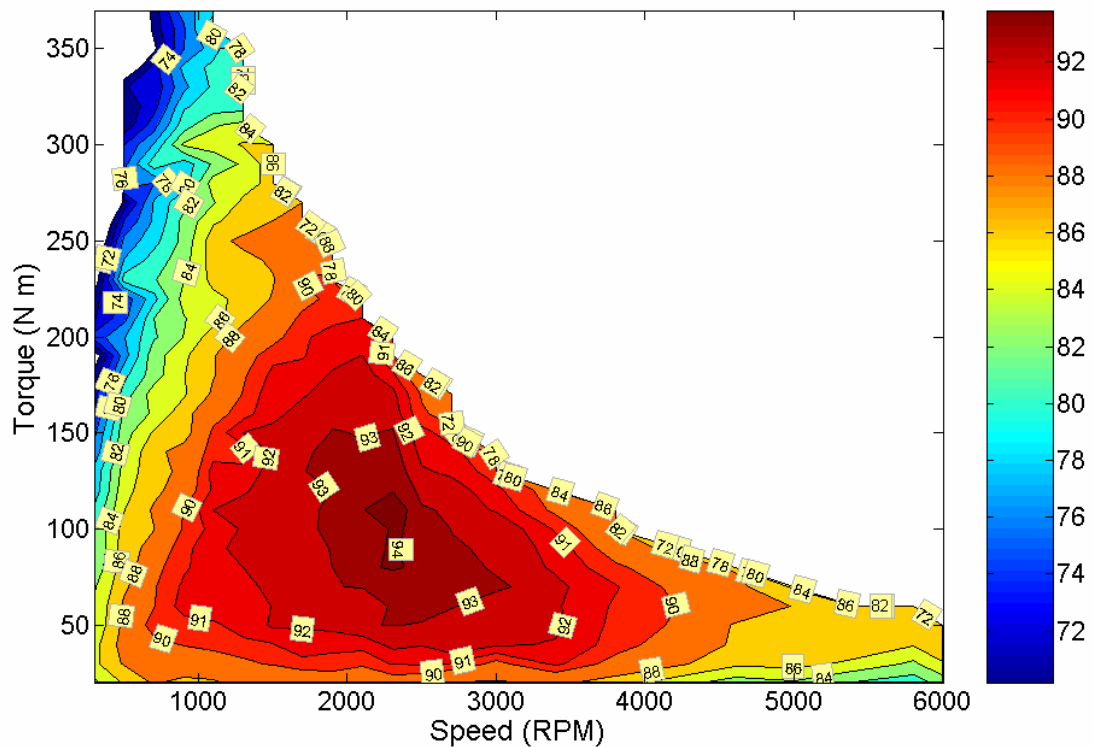Although the dynamometer in this test cell is rated at 150 horsepower, or 112 kilowatts, the low-speed torque capabilities do not match the Prius, due to the nature in which the load torque is developed. An additional PM motor and resistive load bank was used to generate extra low-speed torque. Extremely high stator currents and temperatures were associated with these high torques and the stator winding temperature limitation was increased from 170 to 200 °C to allow for extended data collection periods. Each data point was obtained from a steady state condition maintained for at least 20 seconds to ensure data consistency. Additionally, various negative i_d currents were explored at each operation point to ensure optimal performance. Thus, even with raised temperature limitations, high-torque testing continued to present great difficulties and therefore the temperature of the coolant into the motor was regulated to be below one degree Celsius. Nonetheless, several cool-off periods were still required at high torques.

The sudden increases of efficiency at high torques are due to variance of the stator winding temperatures. For example, at 1100 rpm, the motor was evaluated up to 290 Nm, where the winding temperature reached about 185ºC. Then, the motor was allowed to cool off, and the coolant temperature was lowered from 55ºC to below one degree Celsius. For the next data point at 300 Nm, the average winding temperature was at about 80ºC. Thereafter, the winding temperature increased significantly and the corresponding efficiency decreased to what would be expected if the motor had not been allowed to cool off. Thus, it is observed that up to a two or three percent increase of motor efficiency is caused by excessively high stator winding temperatures.

The inverter efficiency was calculated by dividing the AC output power by the DC input power of the inverter. An inverter efficiency contour map, shown in Figure 4.14, was generated using a technique similar to that used to obtain the motor efficiency contour map. High inverter efficiencies are expected for operation conditions involving high speeds and high currents, in which near maximum inverter voltages are required. During these conditions, the inverter operates in the over-modulation region and the associated switching losses are lower. Although high efficiency inverters are known to reach efficiencies of 98%, concerns arose when inverter efficiencies of 99% began to be indicated.
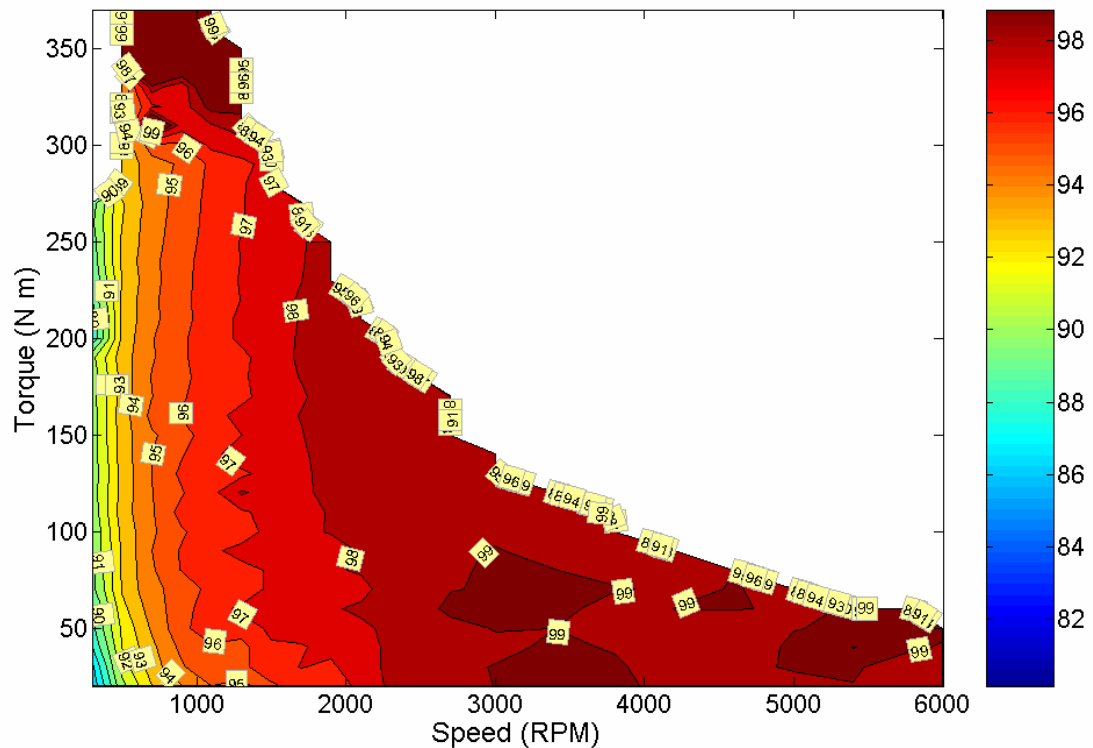

Figure 4.14. Inverter efficiency contour map

An investigation was launched and actions were taken to ensure that all power levels were being measured correctly. This included shortening power leads to the inverter and motor, as well as shortening current and voltage measurement cables. Since the currents into the power meter are low-level representations of the actual current, it was suspected that EMI might be affecting the current measurement. Therefore, tests were conducted with motor currents fed directly through the power analyzer, while ensuring the current rating of power analyzer was not surpassed. The tests were conducted at a high-speed operation point so that the inverter would be in the over-modulation region even for low currents. The measurements closely agreed with data obtained using current transducers and it was concluded that the current measurements were unaffected by EMI. For example, at 4000 rpm and 20 Nm, the inverter efficiency was measured to be 98.6%, compared to 98.8 % measured with the current transducers. Additional steps of measurement verification were taken, and none pointed to any sources of error.

To study the behavior of the entire system, the efficiency data shown in Figures 4.13 and 4.14 were combined to generate the total inverter and motor efficiency contour map shown in Figure 4.15. The appearance of the total efficiency contour map for speeds above 2000 rpm is similar to the motor efficiency contour map, as the inverter efficiency is relatively consistent for these speeds. Below 2000 rpm, the total efficiency drops quickly as the motor speed decreases, yet operations in this region are typically not sustained for extended periods.
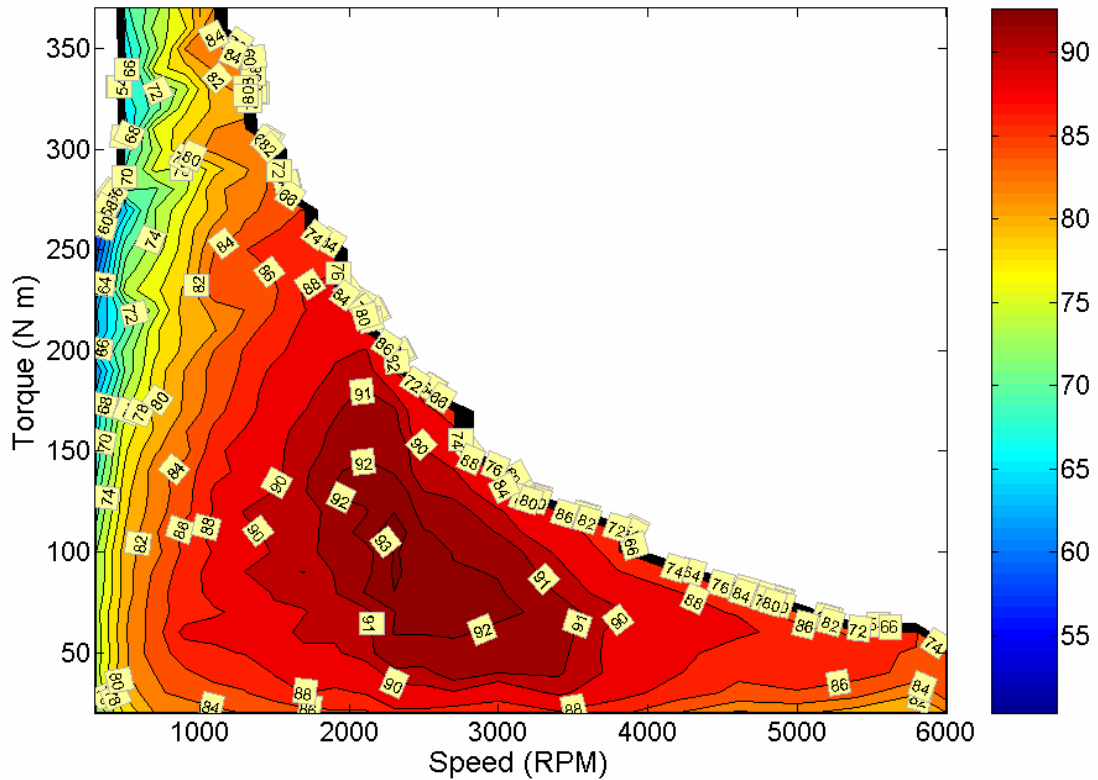
Figure 4.15. Motor and inverter efficiency contour map

4.3 Summary

The details and results of the experimental setup and evaluation have been presented. Parameter identification methods to obtain approximate values for the motor parameters were discussed. A speed and current regulated controller was developed, which requires current, position, and speed feedback signals. Electromagnetic interference (EMI) countermeasures were necessary to obtain stable operation and accurate measurements. Results from Back-EMF and locked rotor tests were used to estimate expected performance and realize the impacts of saturation. The boost converter

was analyzed for efficiency and performance in an isolated set of tests, and was found to have a minimum efficiency of about 97%. Data collected for the most of the torque-speed range of the motor was used to generate efficiency contour maps for the inverter and motor. Although the system nearly met performance expectations in terms of efficiency and peak capabilities, the coolant temperature had to be reduced to maintain the stator winding temperatures within thermal limits.

Chapter 5

Conclusion and Future Work

5.1 Conclusion

The performance characteristics of the 2004 Prius 50 kilowatt motor and inverter have been fully evaluated. Although it is not shown in the efficiency contour maps, data was obtained for torques above 380 Newton-meters. However, it was difficult to operate for the extent of time needed to verify optimal operation and maintain steady state without exceeding thermal limitations, even with a coolant input temperature below one degree Celsius. It was verified that the motor, for a very short amount of time, is capable of producing a peak torque of 400 Newton-meters. Additionally, the instantaneous torque and power ratings as described by Figures 2.5 and 2.6 were verified to be reasonably accurate.

It is important to note that although the motor was operated at the claimed instantaneous power and torque ratings, the actual continuous operation ratings are much lower. An examination of the test results revealed that the continuous power rating of the motor is actually between 17 and 20 kilowatts with 55ºC coolant. The corresponding continuous torque rating is approximately 150 Newton-meters. This is much lower than the objective 30 kW continuous power rating specified by the U.S. Department of Energy FreedomCAR Program. The continuous ratings are especially important for highway driving, where operation conditions are sustained for extended times.

There is not a definite standard by which peak and continuous ratings of torque and power are defined. These ratings depend on various characteristics of the motor and especially the cooling system. The primary source of heat and therefore power loss in the motor are the I^2R losses associated with current through the stator windings. It has been shown that the motor efficiency decreases as the stator winding temperatures increase. As the stator winding temperature increases, the winding resistance also increases. Thus, a torque requiring a certain amount of current will have a greater amount of I^2R losses as the resistance increases. Although the output power remains the same, the input power increases, and the efficiency decreases. Therefore, for the same load level, increased heat loss is associated with the lower performance efficiency. At this load level, if the cooling system cannot dissipate the heat as quickly it is generated, the stator winding temperatures increase and efficiencies decrease more quickly as the two phenomenon build upon each other.

The continuous torque and power ratings correspond with the conditions for which the heat dissipation capability of the cooling system matches the heat generation associated with these maximum performance operation points. Consequently, identical motors with different cooling system characteristics will have different continuous torque and power capabilities. Thus, the environmental conditions in which an HEV operates affect the performance capability of the motor. For example, the actual continuous capacity of the motor would be lower on a summer day in the desert of Nevada when compared to a winter day in Maine.

The peak performance ratings are also be influenced by motor characteristics, cooling system capabilities, and environmental conditions. Additionally, the capabilities of the electrical drive components and time duration of the peak performance should be specified. For example, the absolute maximum torque and power capabilities for sub-second time intervals are likely limited by the ratings of the power electronics. However, driving conditions are not regularly sustained for only sub-second intervals and as the time range under consideration extends, the performance ratings depend more heavily on the capacity of the cooling system. The FreedomCAR and Vehicle Technologies Program of the U.S. Department of Energy has an agenda that includes a peak performance time duration of 18 seconds. Initially, this time value seems extensive, but it may be quite reasonable since vehicles are often accelerated to highway speeds from stopped conditions. Additionally, it is desired that the motor continues to operate after this acceleration demand, and high peak performance ratings will result in reasonable temperatures that allow it to do so.

To optimize system operation, it is crucial to implement an effective cooling system and the control system must incorporate temperature dependent control schemes. The converter-motor efficiencies as well as peak and continuous performance ratings will become increasingly important as the electrical portion of the HEV drive system supplies more of the total power developed at the drive wheels. Improved motor designs will provide a more efficient means of energy conversion and therefore an operation condition will be able to held for a greater extent of time without surpassing thermal limitations.

Although the motor efficiencies were slightly lower than expected, they were found to be above 90% for a large portion of the typical operation regions of the motor, excluding low-speed startup conditions. The inverter efficiencies were surprisingly high and accuracies are calculated to be within one percent, based on the equipment specifications. Although the individual component efficiencies varied from the expected approximate values, the combined inverter and motor efficiencies were close to what were anticipated.

It should be noted that the total motor-inverter efficiencies do not incorporate the entire losses associated with fuel source to drive wheel efficiency. In the 2004 Prius, all energy applied to the drive wheels is obtained from gasoline. An analysis of the entire system should incorporate the efficiencies associated with power generated through the 30-kilowatt generator and inverter, which are expected to have efficiency characteristics similar to that of the 50-kilowatt motor and inverter, as the design and components are similar. Additionally, power loss is also associated with the energy stored in the battery pack, which must also flow through the bi-directional boost converter as enters and leaves the battery pack. If the battery pack has an efficiency of about 90%, the boost converter and battery pack combined have a total efficiency of about 85%. These losses do not occur when the motor is powered directly by the generator, and during regeneration, the energy would be otherwise dissipated as heat in a traditional vehicle. Moreover, the Synergy drive system behaves as a type of continuously variable transmission that is much more efficient than the transmissions used in most vehicles. A combination of these advantages and other technologies has led to an HEV design that is practical in terms of manufacturing costs and driving demands.

5.2 Future Work

There are plenty of opportunities for advancements to be made in areas related to HEV technologies. Toyota already has an HEV on the market with an inverter bus voltage of 650 V and rotor speeds up to 12,500 rpm. Both of these upgrades effectively decrease the current required for a particular torque at the drive wheels, which are connected to the motor through a higher gear ratio. This is especially important for large vehicles, as more energy is required to accelerate a greater mass and increased size typically introduces additional drag and friction losses.

Commercial and developmental technologies continue to be tested to analyze the capabilities and benefits of design techniques and variations. Methods are being developed to incorporate saturation into the motor model in order to develop a more sophisticated controller for dynamic applications. As improvements are made in areas of motor, converter, cooling system, energy storage, and drive system technologies, the practicality of HEVs being the primary means of transportation will continue to increase.

List of References

[1] K. Michiel, et. al., *Energy Management for Vehicle Power Nets*, F2004F368, Technische Universieit Eindhoven, The Netherlands

[2] http://science.howstuffworks.com/fuel-cell5.htm, HowStuffWorks Inc., August 2nd, 2006

[3] http://science.howstuffworks.com/fuel-cell.htm, HowStuffWorks Inc., August 2nd, 2006

[4] C. W. Ayers, et. al., *Evaluation of 2004 Toyota Prius Hybrid Electric Drive System Interim Report*, ORNL/TM-2004/247, the Oak Ridge National Laboratory, 2004.

[5] http://www.toyota.co.jp/en/tech/environment/ths2/index.html, Toyota Motor Corporation, March 14th, 2006

[6] http://john1701a.com, August 29, 2004.

[7] M. Okamura, E. Sato, S. Sasaki, "Development of Hybrid Electric Drive System Using a Boost Converter," Toyota Motor Corporation, 1, Toyota-cho, Toyota, Aichi, 471-8572.

[8] J. Chiasson, *Modeling and High-Performance Control of Electric Machines*, John Wiley & Sons Inc., 2005.

[9] T. M. Jahns, "Flux-Weakening Regime Operation of an Interior Permanent Magnet Synchronous Motor Drive," *IEEE Trans. Ind. Appl.*, vol. IA-23, pp.681-689, July/Aug. 1987.

[10] P. J. Otuday and J. W. McKeever, *Modeling Reluctance-Assisted PM Motors*, ORNL/TM-2005/185, the Oak Ridge National Laboratory, 2006.

[11] T. M. Jahns, G. B. Kliman, and T. W. Neumann, "Interior Permanent Magnet Synchronous Motors for Adjustable-Speed Drives," *IEEE Trans. Ind. Appl.*, vol. IA-22, pp.738-747, July/Aug. 1986.

[12] P. J. Otuday and W. C. Johnson, *The Role of Reluctance in PM Motors*, ORNL/TM-2005/86, the Oak Ridge National Laboratory, 2005.

[13] O. Wallmark, *Thesis on Control of a Permanent Magnet Synchronous Motor with Non-Sinusoidal Flux Density Distribution,* Chalmers University of Technology.

[14] J. S. Lawler, J. M. Bailey, J. W. McKeever, and J. Pinto, "Extending the Constant Power Speed Range of the Brushless DC Motor through Dual-Mode Inverter Control," *IEEE Trans. On Power Electronics*, **19**, (3), May 2004.

[15] J. W. McKeever, J. M. Bailey, S. Das, and J. S. Lawler, *A Preliminary Cost Study of the Dual Mode Inverter Controller*, ORNL/TM-2004/262, the Oak Ridge National Laboratory, 2005.

[16] S. Morimoto, Y. Takeda, T. Hirasa, and K. Taniguchi, "Expansion of Operating Limits for Permanent Magnet Motor by Current Vector Control Considering Inverter Capacity," *IEEE Trans. Ind. Appl.*, vol IA-26, No. 5, Sept./Oct. 1990.

[17] R. H. Staunton, et. al., *Evaluation of 2004 Toyota Prius Hybrid Electric Drive System*, ORNL/TM-2005/178, the Oak Ridge National Laboratory, 2006.

[18] J. S. Hsu, et. al., *Report on Toyota Prius Motor Thermal Management*, ORNL/TM-2005/33, the Oak Ridge National Laboratory, 2005.

Vita

Timothy A. Burress began his work in the field of electronics as he developed troubleshooting skills and learned basic concepts through repairing a wide variety of electronic equipment. Thereafter, he pursued and obtained a Bachelors of Science degree from the University of Tennessee at Knoxville in December 2004. Since June 2004, he has worked with the Power Electronics and Electric Machinery Research Center (PEEMRC) at Oak Ridge National Laboratory (ORNL), where he conducted research in the field of HEV technologies, which includes the work described in this thesis. He received his Masters of Science degree from the University of Tennessee at Knoxville in August 2006, and continues to perform research in areas associated with HEV technologies while working with the PEEMRC at ORNL.